Size-Resolved Dust Direct Radiative Effect Efficiency

Derived from Satellite Observations

Qianqian Song[1,2,*], Zhibo Zhang[1,2], Hongbin Yu[3], Jasper F. Kok[4], Claudia Di Biagio[5],

Samuel Albani[6], Jianyu Zheng[1,2], Jiachen Ding[7]

1. Physics Department, UMBC, Baltimore, Maryland, USA
2. Goddard Earth Sciences Technology and Research II, UMBC, Baltimore, Maryland, USA
3. Climate and Radiation Laboratory, NASA Goddard Space Flight Center, Greenbelt, Maryland, USA
4. Department of Atmospheric and Oceanic Sciences, University of California, Los Angeles, CA 90095, USA
5. Université Paris Cité and Univ Paris Est Creteil, CNRS, LISA, F−75013 Paris, France
6. Department of Environmental and Earth Sciences, University of Milano–Bicocca, Milan, Italy
7. Department of Atmospheric Sciences, Texas A&M University, College Station, Texas, USA

*Correspondence to: Qianqian Song

Email: cd11735@umbc.edu

Abstract

The role of mineral dust aerosol in global radiative energy budget is often quantified by the dust direct radiative effect (DRE). The dust DRE strongly depends on dust aerosol optical depth (DAOD), therefore, DRE efficiency (DREE=DRE/DAOD) is widely compared across different studies to eliminate difference due to the various dust load. Nevertheless, DREE is still influenced by the uncertainties associated with dust particle size distribution (PSD) and optical properties. In this study, we derive a global clear-sky *size-resolved* DREE dataset in both shortwave (SW) and longwave (LW) at top of the atmosphere (TOA) and surface based on satellite observations (i.e., satellite-retrieved dust extinction spatial and vertical distributions). In the DREE dataset, dust geometric diameter from 0.1μm to 100 μm is divided into 10 bins and the corresponding monthly mean DREE (with respect to DAOD at 532nm) for each size bin is derived by using the Rapid Radiative Transfer Model (RRTM). Three sets of state-of-the-art dust refractive indices (RI) and two sets of dust shape models (sphere vs. spheroid) are adopted to investigate the sensitivity of dust DREE to dust absorption and shape. As a result, the size-resolved dust DREE dataset contains globally distributed monthly mean dust DREE at TOA and surface for each of 10 size bins with 5° (longitude) × 2° (latitude) resolution as well as for each dust RI and shape combination. The size-resolved dust DREE dataset can be used to readily calculate global dust DRE for any DAOD and dust PSD, including the uncertainty in the DRE induced by dust microphysical properties (e.g., dust PSD, RI and shape). By calculating dust DRE based on DAOD climatology retrieved from different satellite sensors and based on different dust PSD, we find that uncertainty in the spatial pattern of DAOD induces more than 10% of the uncertainty in SW dust DRE at TOA. The observation-based dust PSD induces around 15%~20% uncertainty in dust DRE at TOA and in the atmosphere. The sensitivity assessments of dust DRE to dust RI and shape

47   further suggest that dust non-sphericity induces a negligible effect on dust DRE estimations, while

48   dust RI turns out to be the most important factor in determining dust DRE, particularly in SW.

49

50

1   Introduction

51

52   Mineral dust is an important component of the atmospheric aerosol (Textor et al., 2006;

53   Choobari et al., 2014). They can influence the radiative energy budget of the Earth-Atmosphere

54   system directly through their interaction with both solar and thermal infrared radiation, which is

55   known as the direct radiative effect (DRE) of dust. The DRE of dust consists of two components.

56   In the solar shortwave (SW) spectral region, dust aerosols reflect a fraction of solar radiation back

57   to the space which generally leads to a negative cooling effect at both top of the atmosphere (TOA)

58   and surface (Tegen et al., 1996; Myhre et al., 2003). In the longwave (LW) thermal infrared region,

59   dust aerosols trap the thermal radiation emitted from Earth's surface by absorption, which

60   generally leads to a positive warming radiative effect at TOA and surface (Sokolik et al., 1998).

61   In addition to DRE, dust can also influence the radiation and the hydrological cycles indirectly

62   through serving as cloud condensation nuclei and ice nuclei and affecting cloud microphysical

63   properties and cloud lifetime, known as indirect effects of dust (Twomey, 1977; Albrecht, 1989).

64   The dust DRE depends on many factors including primarily the atmospheric dust content,

65   represented by its optical depth (DAOD), vertical distribution (especially important for LW DRE),

66   and particles' physico-chemical properties that are the particle size distribution (PSD), complex

67   refractive index (RI), and shape. Besides dust PSD, RI and shape, the dust DRE also depends on

68   the atmospheric composition and structure, notably the atmospheric vertical profile of clouds,

69   water vapor, and temperature, as well as surface properties (Yu et al., 2006). All of these properties

70   vary in space and time and need to be characterized at the best possible spatio-temporal resolution

71   in order to get realistic dust DRE estimates.

72   Among all these factors, DAOD is of first order importance in determining dust DRE since

73   dust DRE is approximately linear with DAOD (Satheesh and Ramanathan, 2000). Many previous

74   studies related to dust DRE are based on DAOD distributions from model simulations. For

75   example, Kok et al. (2017) used four global model simulations to estimate global mean dust DRE

76   efficiency (DREE is defined as DRE/DAOD) and further derive global mean dust DRE. Di Biagio

77   et al. (2020) derived dust DRE based on model-simulated DAOD distributions with global annual

78   mean DAOD constrained by observations. The main advantage of these studies is the availability

79   of continuous and detailed DAOD spatial and temporal variation from model simulations. On the

80   other hand, model-simulated DAOD could be subject to large uncertainties and biases in

81   reproducing DAOD due to parameterizations of various physical processes, therefore need

82   observational constraints for evaluation and improvement.

83   Satellite observations are important sources of data for evaluating model simulations,

84   because of their routine sampling on a global scale and over decadal time periods. Previous studies

85   have developed sensor-specific methods to distinguish dust aerosol from total aerosol based on the

86   size and shape characteristics of dust particles. Some are based on passive satellite observations

87   such as Moderate Resolution Imaging Spectroradiometer (MODIS, Remer et al. (2005)) and others

88   are based on active observations such as Cloud-Aerosol Lidar with Orthogonal Polarization

89   (CALIOP, Winker et al. (2009)). The wide spectral coverage of MODIS measurements allows the

90   retrieval of aerosol particle size information, such as effective radius, fine-mode fraction, aerosol

91   Angstrom exponent, as well as spectral gradient of absorption (Remer et al., 2005; Hsu et al., 2013).

92   Based on the fact that dust aerosols are generally larger in size than other aerosols and have a

93   decreasing absorption from ultraviolet (UV) to the near infrared, the combinations of these

94   retrievals provide the basis for dust separation and dust aerosol optical depth (DAOD) retrievals

95 from MODIS (Kaufman et al., 2005; Ginoux et al., 2012; Voss and Evan, 2020; Yu et al., 2009,

96 2019). In addition, some recent studies have also characterized dust distribution through

97 integrating MODIS measurements with other data sources and model simulations, for example,

98 using the DAOD-to-AOD ratio from MERRA-2 (Modern-Era Retrospective analysis for Research

99 and Applications, version 2), Gkikas et al. (2021) converted the MODIS AOD retrievals to DAOD.

100 However, passive sensors do not provide the vertical structure of aerosol that is critical for studying

101 aerosol–cloud interactions, LW radiative effects and aerosol influences on the thermal structure of

102 the atmosphere (e.g., Meloni et al., 2005, 2015). By contrast, the active sensor CALIOP can

103 provide the vertical profiles of aerosol extinction and particle properties such as depolarization

104 ratio and color ratio, which have been used for improving DAOD retrievals in thermal infrared

105 (TIR) (Zheng et al., 2022) and evaluating global dust simulations (Yu et al., 2010; Wu et al., 2020).

106 The CALIOP dust identification is mainly based on dust aerosols being non-spherical in shape and

107 their linear depolarization ratio being much larger than spherical aerosols (Sakai et al., 2010).

108 Using CALIOP retrievals, Song et al. (2021) derived a three-dimensional (3D) decadal

109 (2007-2019) global scale dust extinction profile climatology, which provides an observational

110 constraint on both the spatial DAOD pattern and the vertical dust distribution for studying dust

111 DRE and evaluating models. In their study, Song et al. (2021) also compared dust retrievals, in

112 particular DAOD, based on different methods (i.e., CALIOP-based and MODIS-based DAOD

113 retrievals), showed that DAOD often differ significantly between the different products and further

114 discussed the potential reasons of causing the differences (e.g., instrument calibration errors and

115 errors in discriminating cloud from aerosol, globally uniform dust Lidar Ratio assumption in

116 CALIOP DAOD retrieval and so on). They showed that DAOD derived from CALIOP

117 observations is generally smaller and more concentrated over 'dust belt' regions - extending from

118 the west coast of north Africa to the Middle East, central Asia, and China - than that derived from

119 MODIS observations. These differences in DAOD in turn lead to different dust DRE estimations,

120 making it difficult to compare different studies to reach meaningful conclusions. Even an

121 agreement of DRE could be a result of the compensation between differences in DAOD and other

122 aforementioned factors, such as dust microphysical properties. Therefore, DRE provides only a

123 weak constraint on model. Instead, a normalized quantity, DRE efficiency (DREE) as the ratio of

124 DRE to DAOD, has been widely used in inter-comparison studies and model evaluations (Di

125 Biagio et al. 2020). Because of the elimination of DAOD, the DREE provides a stronger constraint

126 on dust microphysical properties and their impacts on the dust DRE from different dust source

127 regions (García et al., 2008).

128   In addition to DAOD, dust size is also an important factor in determining dust DRE

129 (Mahowald et al., 2014). Smaller particles are more effective at scattering SW radiation and super-

130 micron particles are more effective at absorbing both SW and LW radiation (Tegen and Lacis,

131 1996).Therefore, when other parameters are equal, fine dust would generally have a more negative

132 SW DRE and a less positive LW DRE than coarse dust. Unfortunately, despite its importance, the

133 simulation of dust PSD in the models and satellite retrievals of dust size remain challenging tasks

134 (Ryder et al., 2019). As a result, there is a large uncertainty in our understanding of dust PSD. For

135 example, several recent studies suggested that model simulations tend to underestimate dust size,

136 especially the very coarse dust with diameter in excess of 5 μm (Adebiyi and Kok, 2020).

137 Moreover, dust RI and shape can be important for DRE estimation as well because besides dust

138 PSD they are the other two factors that determine dust spectral optical properties. As such, it is

139 important to investigate the sensitivity of dust DRE to dust PSD, RI and shape. Previous studies

140 suggest that large dust PSD and RI uncertainty leads to a large uncertainty in dust DRE and thereby

141   DREE estimations. For example, Song et al., (2018) shows that the SW DREE of a dust model

142   with a large size and less absorptive RI is very similar to that of a dust model with a smaller size

143   and more absorptive RI, both in the range of satellite derived values in the NE Atlantic region. Not

144   surprisingly, even DREE cannot provide sufficient constraints due to this possible compensation

145   of effects in the dust PSD and RI.

146   The main objective of this study is to derive a global clear-sky size-resolved dust DREE

147   dataset based on satellite observations and demonstrate its usefulness in constraining, comparing,

148   and understanding the dust DRE estimations. As explained below, the size-resolved DREE

149   decomposes the DREE of dust into several size bins and therefore provide a way to take into

150   account the effects of dust PSD explicitly. The sensitivity of dust DRE to dust RI and shape are

151   also assessed in this study. Due to the inhomogeneous spatio-temporal distribution of those

152   aforementioned factors, it is thus important to consider the spatio-temporal variation of dust DREE.

153   Therefore, we organize the DREE dataset at 5° (longitude) × 2° (latitude) horizontal resolution

154   and at monthly temporal resolution. To the best of our knowledge, this work presents the first such

155   dataset based on retrieved dust properties (i.e., DAOD vertical and horizontal distributions) from

156   satellite observations, although size-resolved DREE from model simulations have been used in

157   previous studies. We will show that our size-resolved DREE can allow users to readily compute

158   the DREE and DRE of dust based on any dust PSD (e.g., from model simulations, satellite

159   retrievals or in-situ measurements). We will also carry out an inter-comparison of the global dust

160   DRE estimations based on different dust PSD and compare the results with previous studies. With

161   these functions, we expect that the size-resolved DREE will be a useful tool for both observational

162   and modeling studies of dust DRE.

163   The rest of the paper is organized as follows. Section 2 provides a description of the data

164   and models used in this study. Section 3 describes the methodology of deriving the size-resolved

165   DREE dataset. In section 4, we describe a methodology of calculating the dust DRE with the size-

166   resolved DREE dataset and its validation. In section 5, we compare the regional and global dust

167   DRE estimations based on different DAOD, dust PSD and compare the results with previous

168   studies. Section 6 provides a summary of the study along with the main conclusions.

2   Data and Models

2.1   Satellite-based DAOD climatology

171   We use CALIOP-based DAOD climatology and dust vertical distribution derived in Song

172   et al. (2021) to derive a size-resolved dust DREE. The reason for choosing CALIOP-based DAOD

173   climatology is discussed in detail in section 3.2. The CALIOP-based dust climatology dataset

174   contains monthly mean DAOD and dust vertical extinction profile on a 5° (longitude) × 2°

175   (latitude) spatial resolution grid for the period 2007-2019. The CALIOP-based DAOD and dust

176   vertical distribution climatology from 2007 to 2010 are used to derive monthly mean size-resolved

177   dust DREE dataset in this study. The selection of 4 years (2007-2010) for DREE calculations is

178   based on several considerations. Firstly, the multi-year DREE calculations allow us to investigate

179   the effect of interannual variations of atmospheric and surface properties to dust DRE. Secondly,

180   this selection is consistent with Song et al. (2018), making it easier to compare our results with

181   previous work. Thirdly, considering the computational efficiency, we do not extend the calculation

182   to more years.

183   In addition to CALIOP-based DAOD climatology, we will use the MODIS-based DAOD

184   climatology to investigate the sensitivity of dust DRE to DAOD spatial pattern in section 5.2. The

185   MODIS-based DAOD climatology achieves global coverage on a 5° (longitude) × 2° (latitude)

186 spatial resolution for the period 2003-2019 by combining the monthly mean Aqua MODIS over-

187 ocean (Yu et al., 2020) and over-land (Pu and Ginoux, 2018) DAOD. In contrast to CALIOP-based

188 DAOD climatology which is based on dust non-sphericity to separate dust aerosol from CALIOP

189 total aerosol observations, MODIS-based DAOD retrieval is mainly based on dust large size to

190 partition DAOD from MODIS total aerosol observations. The two sensor-specific dust partition

191 methods result in different DAOD magnitude and spatial pattern retrievals.

192 Figure 1 shows annual mean DAOD from 2007 to 2010 based on CALIOP and MODIS

193 observations. CALIOP-based and MODIS-based DAOD climatology differ in terms of both

194 magnitude and spatial pattern. MODIS-based DAOD is generally larger than CALIOP-based

195 DAOD. For example, the global $(60°S - 60°N)$ 4-year mean MODIS-based DAOD is 0.047, while

196 CALIOP-based DAOD is 0.032. High DAOD are seen from both CALIOP-based and MODIS-

197 based DAOD over the 'dust belt' regions, where large-scale dust activities occur persistently

198 throughout the year. However, the CALIOP-based DAOD is rather low in some other regions that

199 are known to be dusty in certain seasons, such as South America, Australia, and South Africa. In

200 other words, the two satellite-based DAOD spatial pattern differs significantly with CALIOP-

201 based DAOD more concentrated over 'dust belt' regions.

202
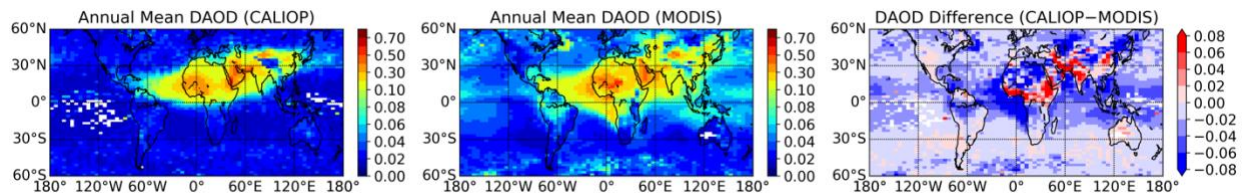
203 Figure 1. Global $(60°S - 60°N)$ spatial pattern of CALIOP-based and MODIS-based 4-year (2007-2010) mean
204 DAOD (Song et al., 2021) and their difference.

205 ## 2.2 Dust physical and optical models

206 To study the sensitivity of dust DREE to dust RI and dust shape, we adopt three sets of

207 dust RI (Figure 2) and two dust shapes and compute a total of 6 sets of DREE based on their

208 combinations. The three dust RI sets represent less absorptive, mean absorptive and more

209 absorptive dust aerosols and the two dust shapes include spherical and spheroidal dust shapes (dust

210 shape distribution is shown in Figure 4 (a) in Song et al. 2018). The mean, 10th and 90th percentile

211 of calculated RI for 19 dust samples over 8 regions in Di Biagio et al. (2019) are used to represent

212 mean, less and more absorptive dust in SW. We combine RI of wavelengths from $0.37\mu m$ to

213 $0.95\mu m$ measured in Di Biagio et al. (2019) and RI of other wavelengths up to $3\mu m$ reported in

214 Balkanski et al. (2007) to get full spectral coverage in SW. The mean, minimum and maximum RI

215 of wavelengths beyond $3\mu m$ measured in Di Biagio et al. (2017) are used to represent mean, less

216 and more absorptive dust in LW. Two dust shapes are used to investigate the effect of dust

217 nonsphericity on dust DRE. One is spherical dust shape, the other one is spheroidal dust shape

218 with dust aspect ratio distribution described by Figure 4 (a) in Song et al. (2018) which is originally

219 from Dubovik et al. (2006). Each combination of dust RI and dust shape is considered as a dust

220 model. As a result, the three dust RI and two dust shapes constitute six dust models in SW and

221 LW, respectively, as shown in Table 1.

222

223
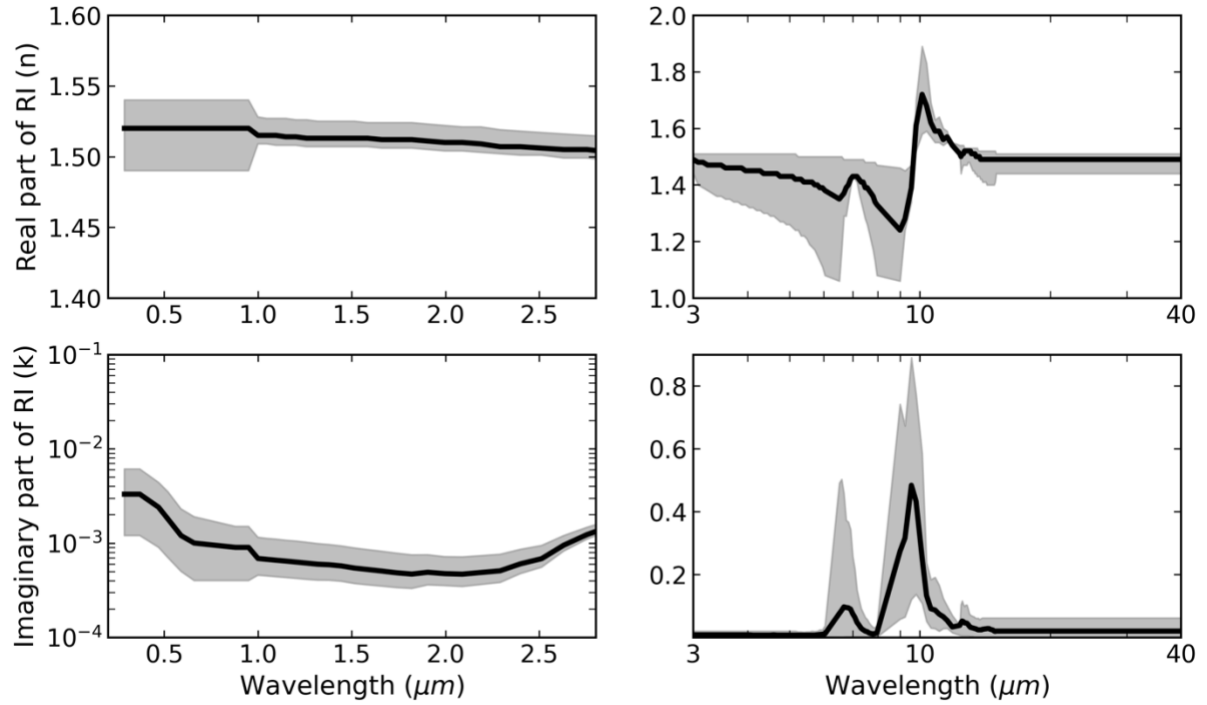
Figure 2. The SW and LW spectral refractive indices (RI) used in this study obtained from Di Biagio et al. (2017,2019) and Balkanski et al. (2007). The black curves represent the mean RI which indicates the mean absorptive dust. The grey shading represents the upper and lower limits indicating more absorptive and less absorptive dust, respectively.

Table 1. Dust models used in this study. Three dust RI are used in shortwave (SW) and longwave (LW) to represent less, mean, and more absorptive dust, respectively. Two dust shape models are used to represent spherical and spheroidal dust shape. The three dust RI sets and two dust shapes constitute 6 dust models in SW and LW respectively.

	SW RI (Balkanski et al. 2007; Di Biagio et al. 2019)			LW RI (Di Biagio et al. 2017)		
	10%	Mean	90%	Minimum	Mean	Maxmum
Sphere	MinSWRI-Sphere	MeanSWRI-Sphere	MaxSWRI-Sphere	MinLWRI-Sphere	MeanLWRI-Sphere	MaxLWRI-Sphere
Spheroid	MinSWRI-Spheroid	MeanSWRI-Spheroid	MaxSWRI-Spheroid	MinLWRI-Spheroid	MeanLWRI-Spheroid	MaxLWRI-Spheroid

230

3   Methodology

3.1   Size-resolved dust scattering properties

Rapid Radiative Transfer Model (RRTM) (Mlawer et al., 1997) is used to compute both SW and LW radiative fluxes for both clean (i.e., cloud-free and aerosol-free) and dusty atmospheres (i.e., free of clouds and non-dust aerosols). RRTM retains reasonable accuracy in

236   comparison with line-by-line results for single column calculations (Mlawer and Clough, 1998;

237   Mlawer et al., 1997). It divides the solar spectrum into 14 continuous bands ranging from 0.2 to

238   12.2 µm and the thermal infrared (3.08–1000 µm) into 16 bands. We explicitly specify the spectral

239   DAOD, single scattering albedo (ω), and asymmetry parameter (g) of dust aerosols for every band

240   in the RRTM radiative transfer simulations. In contrast to radiative transfer scheme in most global

241   models, which do not account for LW scattering, scattering capability is available through the

242   discrete-ordinate-method radiative transfer (DISORT) in RRTM_LW (Stamnes et al., 1988). Four

243   streams are used in DISORT. The Henyey-Greenstein phase function is used and only the first

244   moment of the phase function (i.e., asymmetry parameter) needs to be specified in the RRTM.

245   Dust scattering properties (extinction efficiency Qe, ω and g) depend on several factors

246   including dust PSD, RI, and dust shape. To account for the impact of dust PSD, we divide dust

247   diameters into 10 logarithmically spaced size bins. The 10 size bins represent a wide range of dust

248   geometric diameters (i.e., diameter of a sphere with the same volume) ranging from $0.1 \mu m$ to

249    $100 \mu m$. The geometric diameter (hereafter diameter or D) range of each size bin is listed in Figure

250   3. For each size bin k, the spectral scattering properties ($Qe_k^\lambda, \omega_k^\lambda$ and g_k^λ) are calculated for each

251   dust model shown in Table 1 and each spectral band. In the calculations of scattering properties

252   ($Qe_k^\lambda, \omega_k^\lambda$ and g_k^λ), dust particle number (dN/dD) is assumed to be uniformly distributed within

253   each size bin. We use the Lorenz–Mie theory code of Wiscombe (1980) to compute the spectral

254   optical properties of dust particles in the assumption of sphericity. The spectral optical properties

255   of spheroidal dust particles are derived from the database of Meng et al. (2010). Figure 3 shows

256    $Qe_k^\lambda, \omega_k^\lambda$ and g_k^λ for MeanSWRI-MeanLWRI-Spheroid dust model. In SW, finer dust has a larger

257   ω and smaller g, implying a more effective SW backscattering of finer dust. As a result, finer dust

258   is expected to have stronger cooling effect (more negative DREE values) at TOA generally. In

259 LW, $\frac{Qe_k^{10\mu m}}{Qe_k^{532nm}}$ is generally enhanced as dust size increases, which implies that coarser dust has larger

260 extinction in LW (optically represented by $DAOD^{10\mu m}$) than finer dust when $DAOD^{532nm}$ is

261 constrained by CALIOP retrieval. As a result, larger $DAOD^{10\mu m}$ will enhance the LW warming

262 (more positive LW DREE) at TOA of coarser size bins. On the other hand, the increased ω and g

263 of the coarser size bins indicates stronger forward scattering, which reduces the enhancement in

264 LW warming induced by larger $DAOD^{10\mu m}$.
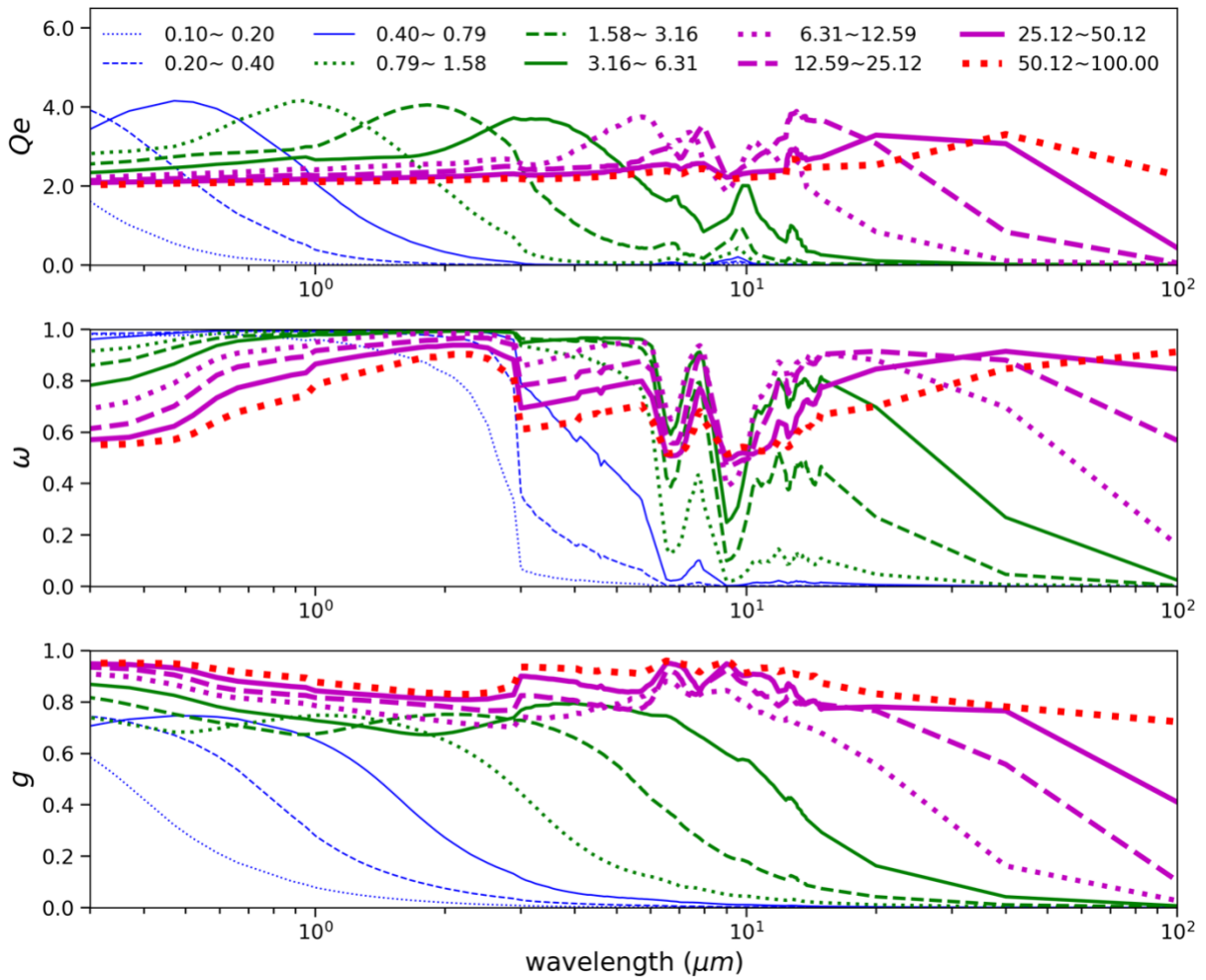
265

266 Figure 3. Spectral scattering properties (i.e., Q_e: extinction efficiency, ω: single scattering property, g: asymmetry
267 parameter) of each size bin for the MeanSWRI-MeanLWRI-Spheroid dust model. The scattering properties of each
268 size bin are represented by the corresponding curve indicated in the legend. Each size bin is defined with respect to
269 dust diameter with unit of micrometers (μm).

270 ## 3.2 DREE dataset

271   Based on the dust scattering properties shown in Figure 3 and the procedures summarized

272 in Figure 4, we compute the size-resolved dust DREE for the MeanSWRI-MeanLWRI-Spheroid

273 dust model in SW and LW. In this section, we focus on demonstrating the method of deriving size-

274 resolved dust DREE for one dust model, but this method is applicable to all six dust models listed

275 in Table 1.

276   First, we use RRTM to simulate monthly mean dust DRE from 2007 to 2010 for each 5°

277 (longitude) $\times$ 2° (latitude) grid with CALIOP-based $DAOD^{532nm}$ exceeding 0.01. The

278 $DAOD^{532nm}$>=0.01 threshold ensures most dusty regions over the globe are covered (see Figure

279 S1 and Figure S2 in the Supplement) and in the meanwhile balances the computational cost. Dust

280 DRE are calculated for each size bin using the extinction properties of the corresponding size bin

281 shown in Figure 3 (denoted as $DRE_{k,i,j}$, hereafter k indicates size bin index and (i,j) indicates

282 longitude-latitude grid index, unless specified otherwise). Note that we do not consider dust RI

283 spatial variation and dust size vertical variation due to the lack of observation-based dust

284 minerology and size estimation on global scale. In $DRE_{k,i,j}$ calculations, we constrain the monthly

285 mean dust extinction vertical distributions using the CALIOP-based climatological dataset of Song

286 et al. (2021). Worth to mention, our target in this section is $DREE_{k,i,j}$ calculations. Considering

287 dust DRE is approximately linear to DAOD (Satheesh and Ramanathan, 2000), the DAOD used

288 in dust DRE calculations will not affect dust DREE results significantly, we simply calculate dust

289 $DRE_{k,i,j}$ with respect to $DAOD_{i,j}^{532nm}$ from CALIOP-based DAOD climatology. As a result,

290 $DRE_{k,i,j}$ calculated in this section are only intermediate variables used to calculate dust DREE,

291 they do not represent actual DRE contributed by k[th] size bin. The atmospheric profiles such as

292 water vapor (H₂O), ozone (O₃) and temperature (T_{atm}) vertical profiles of 72 levels are from 3-

293 hourly MERRA2 assimilated meteorological fields data (Gelaro et al., 2017). We combine the 1-

294 hourly surface albedo for visible beam from MERRA2 radiation diagnostics with the instantaneous

295 spectral surface albedo from the integrated CALIPSO, Cloud-Sat, CERES, and MODIS merged

296 product (CCCM) (Kato et al., 2011) to get time-dependent spectral surface albedo. Surface

297 temperature is obtained from 1-hourly MERRA2 radiation diagnostics data. The atmospheric and

298 surface properties are all aggregated to monthly mean values at eight UTC times: 0:30, 3:30, 6:30,

299 9:30, 12:30, 15:30, 18:30, 21:30 to obtain monthly-mean diurnal cycle for radiative transfer

300 simulations. Considering DRE^{SW} strongly depends on solar zenith angle (SZA), we calculate

301 DRE^{SW} for every 1 hour using the corresponding hourly SZA in midmonth day. As a result, every

302 three SZA share the same atmospheric and surface properties in DRE^{SW} calculations due to their

303 different temporal resolution.

304 Table 2 List of definitions of variables and their indices.

Variable	Definition
k	size bin index
i, j	longitude-latitude grid index
t	8 UTC times with 3-hour interval (i.e., 0:30, 3:30, 6:30, 9:30, 12:30, 15:30, 18:30, 21:30)
tt	24 UTC times with 1-hour interval
day^{mm}	The midmonth day of the month
$\overline{R(t)}, \overline{H_2O(t)}, \overline{O_3(t)},$ $\overline{CO_2(t)}, \overline{T_{atm}(t)}$	3-hourly monthly mean surface albedo and vertical profile of water vapor, ozone, carbon dioxide and atmospheric temperature
ζ_d	dust properties such as DAOD, dust extinction vertical profile and scattering properties
$\overline{_{1h}DRE^{SW}_{k,i,j}(tt)}$	1-hourly monthly mean DRE^{SW} (i.e., monthly mean DRE^{SW} at each of 24 UTC times) of kth size bin and (ith, jth) grid
$\overline{_{3h}DRE^{LW}_{k,i,j}(t)}$	3-hourly monthly mean DRE^{LW} (i.e., monthly mean DRE^{LW} at each of 8 UTC times) of kth size bin and (ith, jth) grid
$\overline{DRE^{SW}_{k,i,j}}, \overline{DRE^{LW}_{k,i,j}}$	The monthly and diurnally mean dust DRE^{SW} and DRE^{LW} of kth size bin and in (ith, jth) grid
$\overline{DREE_{k,i,j}}$	The monthly and diurnally mean dust DREE^{SW} and DREE^{LW} of kth size bin and (ith, jth) grid
$\overline{DAOD^{532nm}_{i,j}}$	The monthly mean dust optical depth at 532nm of (ith, jth) grid

305

306   The definitions of variables and indices used to derive size-resolved dust DREE dataset are

307 summarized in Table 2. Eq. (1) shows the way of deriving 1-hourly monthly mean DRE^{SW}.

$$\overline{_{1h}DRE_{k,i,j}^{SW}(tt)} = DRE_{k,i,j}^{SW}\left(\overline{R(t)},\overline{H_2O(t)},\overline{O_3(t)},\overline{CO_2(t)},\ \zeta_d,\ SZA(day^{mm},tt)\right), \tag{1}$$

308   where 't' indicates 8 UTC times with 3-hour interval. 'tt' indicates 24 UTC times with 1-hour

309   interval. 'day^{mm}' indicates the midmonth day of the month, and '$\overline{R(t)}$' represents 3-hourly

310   monthly mean surface albedo. We include 3-hourly monthly mean vertical profile of water vapor,

311   ozone, carbon dioxide ($\overline{H_2O(t)},\overline{O_3(t)},\overline{CO_2(t)}$) to account for gaseous absorption. The temporal

312   resolution inconsistency of SZA as well as atmospheric and surface properties requires every three

313   SZA share the same atmospheric and surface properties in the calculations. 'ζ_d' represents dust

314   properties such as DAOD, dust extinction vertical profile and scattering properties which are

315   independent of UTC time in our calculations. Dust extinction vertical profile is interpolated to the

316   72 levels in consistency with vertical profiles of water vapor, ozone and temperature from

317   MERRA2.

318   Eq. (2) shows the way of deriving 3-hourly monthly mean DRE^{LW}.

$$\overline{_{3h}DRE_{k,i,j}^{LW}(t)} = DRE_{k,i,j}^{LW}\left(\overline{E},\overline{H_2O(t)},\overline{O_3(t)},\overline{CO_2(t)},\overline{T_{atm}(t)},\zeta_d\right) \tag{2}$$

319   Surface spectral emissivity ('E') is obtained from Huang et al. (2016), which contains

320   monthly mean spectral surface emissivity with 0.5-degree spatial resolution based on MODIS-

321   retrieved mid-IR surface emissivity and modeled different types of surface spectral emissivity.

322    $\overline{T_{atm}(t)}$ represents 3-hourly monthly mean vertical profile of atmospheric temperature. With the

323   aid of the 3-hourly monthly mean atmospheric properties, monthly mean DRE^{LW} is calculated for

324   every 3 hours.

325   Then the 1-hourly monthly mean dust DRE^{SW} ($\overline{_{1h}DRE_{k,i,j}^{SW}(tt)}$) derived from Eq. (1) is

326   averaged diurnally (over 24 points) to get the monthly and diurnally mean dust DRE^{SW} ($\overline{DRE_{k,i,j}^{SW}}$)

327   as indicated by Eq. (3).

$$\overline{DRE_{k,i,j}^{SW}} = \frac{\sum_{tt} \overline{_{1h}DRE_{k,i,j}^{SW}(tt)}}{\sum tt} \tag{3}$$

328

329   Similarly, the 3-hourly monthly mean DRE^{LW} ($\overline{_{3h}DRE_{k,i,j}^{LW}(t)}$) derived from Eq. (2) is

330 averaged diurnally (over 8 points) to get the monthly and diurnally mean dust DRE^{LW} ($\overline{DRE_{k,i,j}^{LW}}$) as

331 indicated by Eq. (4).

$$\overline{DRE_{k,i,j}^{LW}} = \frac{\sum_{t} \overline{_{3h}DRE_{k,i,j}^{LW}(t)}}{\sum t} \tag{4}$$

332   The method described by Eq. (1) - Eq. (4) will be referred to as the '*conventional*' method

333 of calculating monthly mean dust DRE in Section 4.

334   Based on the monthly mean size-resolved dust DRE^{SW} ($\overline{DRE_{k,i,j}^{SW}}$) and DRE^{LW} ($\overline{DRE_{k,i,j}^{LW}}$), we

335 derive the monthly mean size-resolved dust DREE ($\overline{DREE_{k,i,j}}$) using Eq. (5) for SW and LW

336 respectively. Note that the monthly mean size-resolved dust DREE ($\overline{DREE_{k,i,j}}$) is calculated by

337 dividing by monthly mean $DAOD^{532nm}$ since the size-resolved $\overline{DRE_{k,i,j}}$ was initially derived with

338 respect to monthly mean $DAOD^{532nm}$.

$$\overline{DREE_{k,i,j}^{SW\,or\,LW}} = \frac{\overline{DRE_{k,i,j}^{SW\,or\,LW}}}{\overline{DAOD_{i,j}^{532nm}}} \tag{5}$$

339   Finally, we average the monthly mean size-resolved dust DREE ($\overline{DREE_{k,i,j}}$) over 4 years

340 to get monthly mean size-resolved dust DREE datasets in addition to the associated interannual

341 standard deviation (std). The std indicates the DREE uncertainty caused by interannual variation

342 of monthly mean atmospheric and surface properties as well as dust vertical distribution. Finally,

343 the dataset developed in this study contains monthly mean size-resolved dust DREE and its

344 associated interannual std at TOA and surface with dimension of 10 bins, 12 months, 90 latitudes,

345   72 longitudes for each of six dust models in SW and LW respectively. Figure S1 and Figure S2 in

346   the Supplement demonstrate the global distribution of the monthly mean size-resolved DREE^{SW}

347   and DREE^{LW} at TOA for June.

348   It is important to note that dust DREE of each grid cell rarely depends on the DAOD

349   because dust DRE is approximately linear with DAOD (Satheesh and Ramanathan, 2000).

350   Therefore, the choice of CALIOP- or MODIS-based DAOD climatology to derive the global

351   ($5° \times 2°$) size-resolved DREE dataset will not lead to large difference. In other words, the size-

352   resolved DREE dataset is rarely related to the robustness of the DAOD used in the derivation

353   process. We select CALIOP-based DAOD to derive the size-resolved dust DREE dataset because

354   that the CALIOP-based dust climatology contains dust vertical distribution, which is especially

355   important for obtaining LW DREE. Nevertheless, using CALIOP-based dust retrieval to derive

356   size-resolved dust DREE dataset has several limitations: (1) The size-resolved dust DREE dataset

357   may miss some regions with tenuous dust layers that below the CALIOP sensitivity. (2) The LW

358   DREE is related to the quality of dust vertical distribution retrieval. By contrast, dust DRE highly

359   depends on DAOD, therefore we will use different DAOD climatological datasets retrieved from

360   different sensors (i.e., CALIOP and MODIS) to investigate global dust DRE in section 5.2.

361   Furthermore, even though dust DREE of each grid cell is rarely related to DAOD, regional or

362   global mean dust DREE will depend on the DAOD spatial distribution (i.e., DAOD 2D distribution)

363   in the region of interest (see details in section 5.2).

364   Based on the monthly mean size-resolved dust DREE datasets derived above, we further

365   calculate globally annual mean size-resolved dust DREE^{SW} and DREE^{LW} at TOA and surface for

366   the six dust models (Figure 5). As discussed above, the global mean dust DREEs depends on the

367   DAOD spatial distribution, the global mean dust DREEs shown in Figure 5 is based on CALIOP-

368 based DAOD spatial distribution from Song et al. (2021). Generally smaller bins cause stronger

369 cooling in SW and less warming in LW, which is consistent with our discussions in 3.1. This

370 observationally informed globally annual mean size-resolved dust DREE is also consistent with

371 the model-simulated results shown in supplementary Figure S3 in Kok et al. (2017) in terms of the

372 variation trend of DREE with respect to dust size. Moreover, our study explicitly shows the

373 sensitivity of dust DREE to dust RI and dust shape. For example, Figure 5 shows that DREE^{SW} is

374 strongly sensitive to dust RI as DREE^{SW} of different dust RI is widely separated. Depending on

375 dust RI, DREE^{SW} switches from cooling effect (negative value) to warming effect (positive value)

376 at different size bins. More absorptive dust starts to warm the Earth system in SW at smaller dust

377 size, and vice versa. In addition, our results suggest that DREE^{SW} is generally not sensitive to dust

378 shape. Specifically, dust shape is not important for DREE^{SW} in most size bins, while it is important

379 in the fourth size bin ($D: 0.79\mu m \sim 1.58\mu m$) with DREE^{SW} of spheroidal dust obviously higher

380 (less negative) than spherical dust. In the DREE^{LW}, dust shape is almost as important as RI for

381 several size bins.
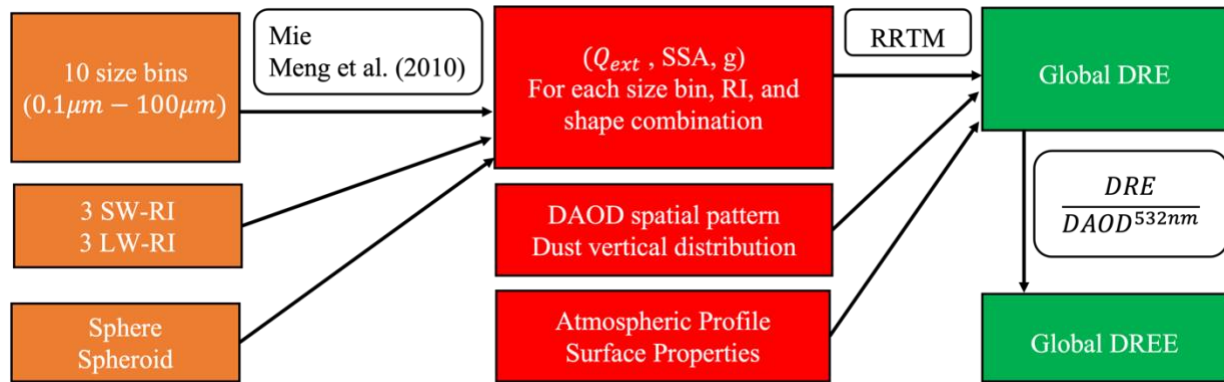
383 Figure 4. Schematic of the methodology used to derive size-resolved dust DREE dataset. Orange boxes denote dust
384 models used to calculate dust scattering properties. Red boxes denote inputs for RRTM. Green boxes denote outputs
385 from RRTM.

386
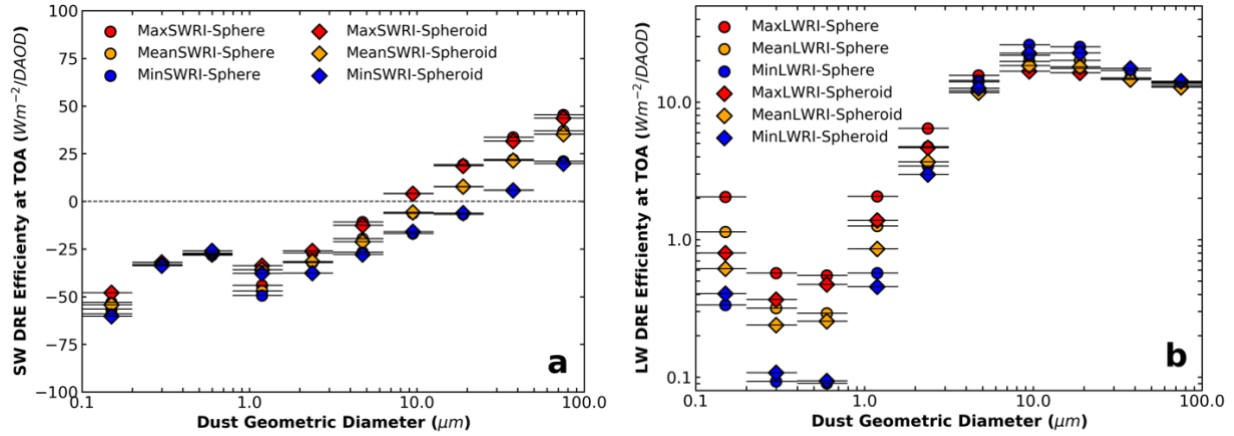
Figure 5. Globally annual mean size-resolved dust DREE in SW (**a**) and LW (**b**) for six dust models (six markers). Horizontal bars indicate the dust diameter range of each size bin. Note: LW DREE is on a logarithm scale; in contrast to global model simulations, we consider dust LW scattering in LW DRE Efficiency calculations.

Our size-resolved dust DREE dataset is unique in many aspects: First, our DREE dataset is derived based on CALIOP-based dust 3D distribution. Size-resolved DREE is derived for all grids with CALIOP-based DAOD >= 0.01. Second, our size-resolved DREE dataset covers a wide range of dust diameters, specifically, they include dust DREE for ten dust diameter size bins ranging from $0.1 \mu m$ to $100 \mu m$. This is challenging, if not impossible, to obtain from global models because these models generally simulate dust particles with diameter only up to $20 \mu m$ and coarse dust particles in models deposit quickly and could not be sustained to the remote transport regions (Huneeus et al., 2011; Adebiyi and Kok, 2020) where coarse particles have been observed by in-situ measurements (Weinzierl et al., 2017). As a result, our size-resolved DREE dataset achieves a wide spatial coverage for a large range of dust size. This is critical for investigating impacts of coarse dust and even giant dust particles on dust DRE on both regional and global scales. Third, considering that the dust vertical distribution is important for quantifying DREE[LW], we constrain dust vertical distribution using CALIOP-based dust retrievals in DREE[LW] computation. Fourth, our size-resolved dust DREE dataset accounts for dust LW scattering in DREE[LW] calculations since scattering capability is available through the DISORT in RRTM_LW (Stamnes

405 et al., 1988). Dufresne et al., (2002) suggests that dust LW scattering enhances dust LW warming

406 effect at TOA by a factor of up to 50%. However, dust LW scattering is generally not considered

407 in most global models. Therefore, many previous studies artificially account for dust LW scattering

408 by increasing the radiative perturbation due to LW absorption by a certain fraction. For example,

409 Kok et al. (2017) accounts for LW scattering by artificially augmenting DRE^{LW} by 23% and Di

410 Biagio et al. (2020) augmented DRE^{LW} by 50%.

411   On the other hand, our size-resolved dust DREE dataset has several limitations. First,

412 possible vertical and horizontal variations of dust particle size in each grid box (5° × 2°) are not

413 accounted for in our calculation. The entire dust-loading column in each grid box is assumed to

414 have the same dust size distribution. Second, we do not explicitly account for spatial variation of

415 dust RI, in other words, dust RI is assumed to be globally uniform. This uncertainty is assessed

416 through the sensitivity tests of DREE to dust RI using three sets of state-of-the-art dust RI based

417 on laboratory measurement of 19 dust samples all over the world. Third, dust 3D distribution in

418 the DREE calculation is constrained by CALIOP observations. The limits on the sensitivity of

419 CALIOP will affect the 3D distribution of dust in our calculation. Fourth, we account for dust

420 nonsphericity by using spheroidal shape model. This shape can't perfectly represent the highly

421 irregular shape and roughness of real dust. In addition, several studies suggest that dust non-

422 sphericity is underestimated by the spheroidal shape model (Huang et al., 2020). The spheroidal

423 shape model assumption thus might produce systematic errors.

424   Overall, the size-resolved dust DREE dataset is useful in many dust-related studies. First,

425 with our size-resolved dust DREE dataset, dust DRE could be calculated efficiently for any DAOD

426 magnitude, DAOD spatial pattern and any dust PSD for any regions or the globe (see details in

427 Section 4.1). Second, our size-resolved DREE dataset is derived for different RI and different dust

428   shapes respectively. As a result, we could estimate dust DRE uncertainty coming from DAOD,

429   PSD, RI, and shape separately to better understand major uncertainty sources in dust DRE

430   estimations. Third, our size-resolved DREE dataset could be used to evaluate model simulated

431   DREE for each size bin.

4   DRE calculation methodology and its validation

4.1   DRE calculation based on DREE dataset

434   With the size-resolved dust DREE dataset derived in section 3.2, DRE of dust with any

435   PSD and DAOD could be computed very efficiently without performing radiative transfer

436   simulations as we do in *conventional* method. This section introduces the methodology of applying

437   the size-resolved DREE dataset to calculate DRE of dust with any PSD and DAOD.

438   DRE of full-size range of dust can be expressed as the sum of DRE from each size bin

439   (DRE_k). Dust DRE_k is approximated to be linearly proportional to DAOD of kth size bin ($DAOD_k$)

440   (Satheesh and Ramanathan, 2000). The similar concept of calculating dust DRE has been used in

441   previous studies e.g., Kok et al. (2017). Eq. (6) shows the process of computing dust DRE using

442   the size-resolved DREE dataset.

$$DRE = \sum_k DRE_k = \sum_k DREE_k \times DAOD_k = \sum_k DREE_k \times f_k \times DAOD, \qquad (6)$$

443   where DRE represents dust DRE induced by full size range of dust with optical depth of $DAOD$.

444   f_k is the fraction of the DAOD contributed by the kth size bin.

445   Each variable in Eq. (6) can be obtained or derived from datasets developed in this study

446   and other studies. For example, the size-resolved DREE dataset ($DREE_{k,i,j}$) derived in this study

447   is essential for utilizing this efficient and novel DRE calculation method. DAOD can be obtained

448   from CALIOP-based or MODIS-based DAOD climatological datasets (Song et al., 2021). f_k can

449   be derived from dust extinction efficiency (Qe), the geometric cross-sectional area (A) and dust

450   PSD (dN/dD) based on Eq. (7).

$$f_k \equiv \frac{DAOD_k}{DAOD} = \frac{\int_{D^{k-}}^{D^{k+}} Qe^{532nm}(D)A(D)\frac{dN}{dD}dD}{\int_0^{D^{max}} Qe^{532nm}(D)A(D)\frac{dN}{dD}dD} \tag{7}$$

451   Qe is defined according to $Qe \equiv \frac{\sigma_e}{A}$, where σ_e is extinction cross section, the geometric

452   cross-sectional area of the particle (A) can be expressed as $A = \pi r^2$. Under the assumption of

453   spherical dust particle, r is the radius. Under the assumption of spheroidal dust particle, Vouk

454   (1948) shows that the average projected area of a convex body (e.g., spheroidal particle) is $A =$

455   πr^2, where r is the radius of a surface area-equivalent sphere. The average is taken over all

456   possible orientations in space, which is consistent with our assumption of randomly oriented dust

457   particles in the atmosphere. $Qe^{532nm}(D)$ for the six dust models are shown in Figure 6 (a), they

458   all converge to 2 as the dust diameter becomes much larger than the wavelength, which is

459   consistent with the principle of geometric optics (van de Hulst, 1957). By contrast, $Q_e^{550nm}(D)$ of

460   non-spherical dust in Kok et al. (2017) has a much larger value than spherical dust for dust $D \geq$

461   $1\mu m$ (see their Figure 1(b)). This discrepancy is probably due to the different Q_e definitions used

462   in the two studies. Kok et al. (2017) defined Q_e as dust extinction per unit cross section of volume-

463   equivalent sphere. Figure 6 (b) shows that f_k of a specific PSD is not sensitive to dust RI and dust

464   shape, this is also suggested by the similar Qe^{532nm} v.s. geometric diameter (D) trends of the six

465   dust models shown in Figure 6 (a). In contrast, f_4 (i.e., f_k for the fourth size bin with D ranging

466   from $0.79\mu m \ to \ 1.58\mu m$) is more sensitive to dust shape than other size bins, this is in line with

467   the larger difference in Qe^{532nm} with shape shown in Figure 6 (a).

468
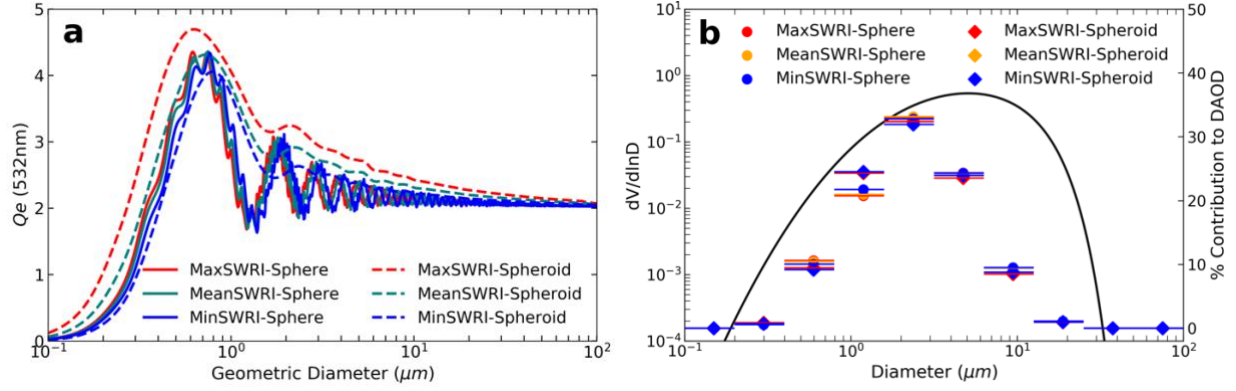
Figure 6. (**a**) Dust extinction efficiency (Qe) at 532nm for six dust models. (**b**) The colorful bars represent f_k calculated for six dust models based on a specific dust PSD ($dV/dlnD$) indicated by black curve. Note, f_k is not sensitive to different dust models such as dust RI and dust shape.

In summary, the size-resolved dust DREE dataset provides an efficient way to compute DRE for any dust PSD and any DAOD by using Eq. (6) and Eq. (7). To distinguish from the *conventional* method introduced in section 3.2, this method of calculating dust DRE based on size-resolved DREE dataset is referred to as '*DREE-integration*' method.

4.2   Validation of DRE calculation methodology

In this section, we select the Sahara Desert ($14°N$-$30°N$, $15°W$-$30°E$) to validate the *DREE-integration* method. We choose MeanSWRI-MeanLWRI-Spheroid dust model and Fennec-Fresh dust PSD (see red curve in Figure 7) measured within 12h of dust uplift in remote Sahara locations by Fennec field campaign to represent microphysical properties of Saharan dust (Ryder et al., 2013a, b). Monthly mean DAOD is from CALIOP-based DAOD climatology.

482
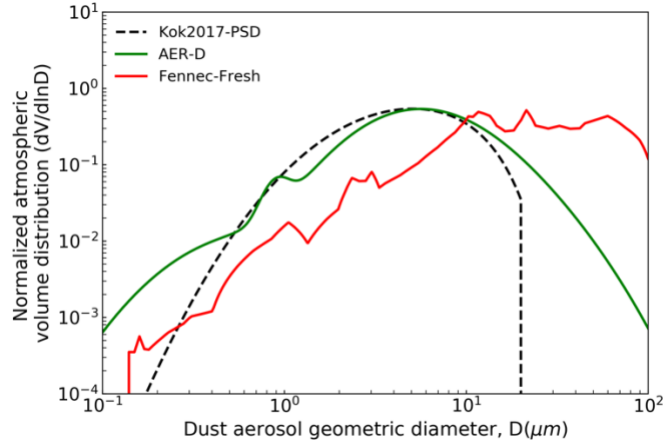
Figure 7. Normalized atmospheric dust volume distribution (dV/dlnD) described in Table 5 (Kok et al., 2017; Ryder et al., 2013a; b; 2018; 2019).

Figure 8 shows the comparison of 4-year (2007-2010) monthly mean dust DRE between the *Conventional* and *DREE-integration* method. In Conventional DRE calculation, dust scattering properties (Qe, ω and g) are calculated based on the Fennec-Fresh PSD and then used to calculate monthly mean dust DRE from 2007 to 2010 with RRTM as described in Section 3.2 (Eq. 1 – Eq. 4). While the DREE-integration method is based on the monthly mean size-resolved DREE dataset derived based on 4-year (2007-2010) data as described in Section 4.1 (Eq. 6 – Eq. 7). The excellent agreement in monthly mean dust DRE between two methods validates the *DREE-integration* DRE calculation methodology.

493

494
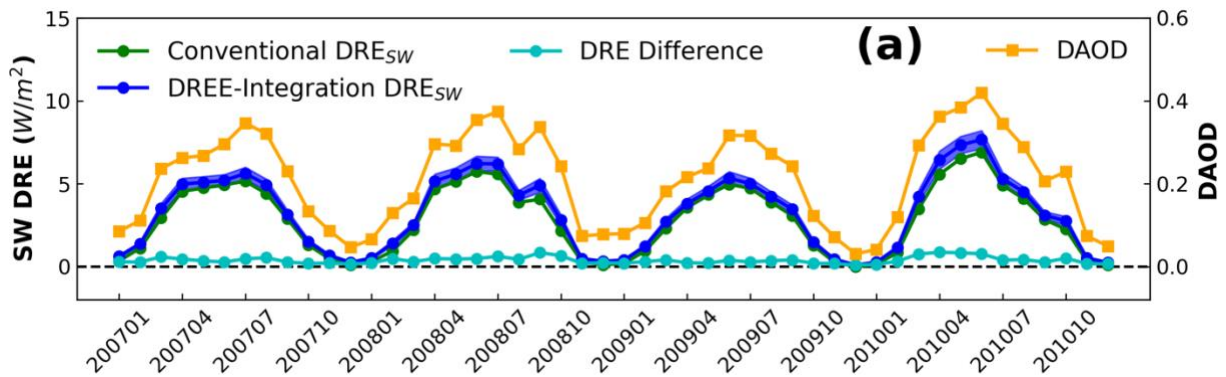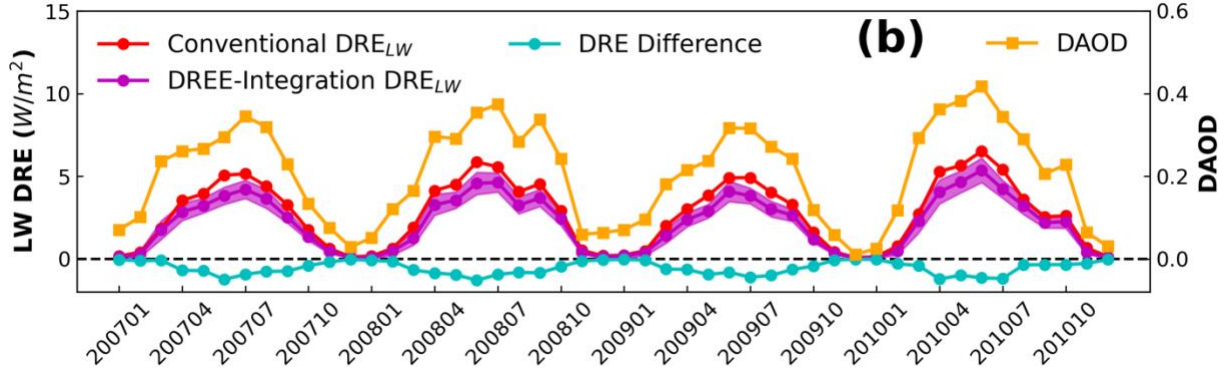
495 Figure 8. Monthly mean dust DRE^{SW} (**a**) and DRE^{LW} (**b**) comparison between *Conventional* and *DREE-integration*
496 calculation from 2007 to 2010 over Sahara Desert. The DRE Difference line represents the difference between *DREE-*
497 *integration* and Conventional calculation. Shaded area along *DREE-integration* DRE indicates the one standard
498 deviation caused by the atmospheric and surface variations as well as dust vertical distribution variation within the
499 four years. Orange curves indicate CALIOP-based monthly mean DAOD. The variation of dust DRE match well with
500 DAOD variation.

501   The shaded-area associated with DREE-integration DRE corresponds to the one standard

502 deviation of DREE caused by the 4-year (2007-2010) interannual variation of factors except dust

503 microphysical properties such as monthly mean atmospheric and surface properties as well as dust

504 vertical distributions (hereafter those factors is referred to as non-dust-factors for short). The

505 narrow shaded-area along DREE-integration DRE suggests non-dust-factors cause very small

506 uncertainty in dust DRE estimations. However, the small effects of 4-year interannual variation of

507 non-dust-factors may not necessarily be representative due to the limited number of years

508 considered. Section 2.1 discusses in detail for the reason of choosing 2007-2010 to derive size-

509 resolved DREE dataset. To check the representative of 4-year interannual variation for non-dust-

510 factors, we compare the 4-year (2007-2010) and 10-year (2007-2017) interannual standard

511 deviation (std) of monthly mean non-dust-factors (e.g., surface albedo, surface temperature and

512 dust vertical distribution) in Figure 9. To evaluate the interannual variation of dust vertical

513 distribution, we define dust mean extinction height (Z_α) referring to Koffi et al. (2012) as $Z_\alpha =$

514 $\frac{\sum_{i=1}^{n} \beta_{ext,i} \times Z_i}{\sum_{i=1}^{n} \beta_{ext,i}}$, where $\beta_{ext,i}$ is the dust extinction coefficient at 532nm at level *i,* and Z_i is the altitude

515 of level *i*. Nevertheless the 10-year std is slightly larger than 4-year std, they are both close to zero

516   and on the same order of magnitude. As such, even though our monthly mean size-resolved DREE

517   dataset is derived from 4-year (2007-2010) data, they could be used to represent DREE and

518   calculate DRE for other years considering the small sensitivity of monthly mean dust DRE to

519   interannual variation of non-dust-factors.

520
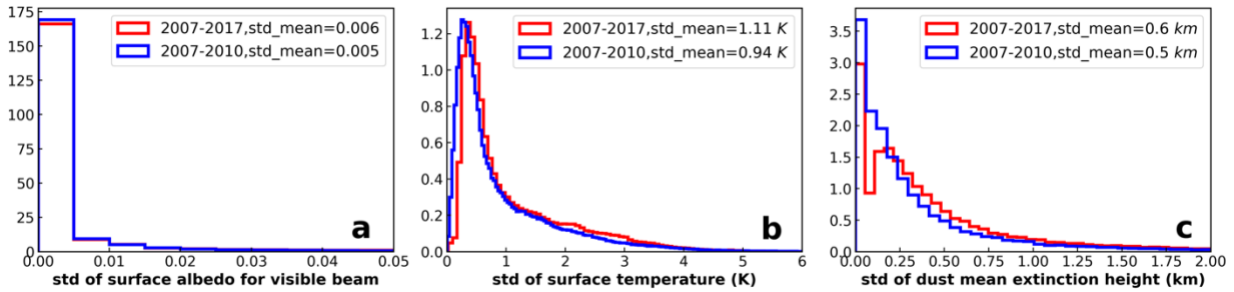
521   Figure 9. Probability density function (PDF) of 4-year and 10-year interannual standard deviation (std) in monthly
522   mean (**a**) surface albedo, (**b**) surface temperature, and (**c**) dust mean extinction height. The PSD analyses include
523   interannual std in 12 months and all 5° (longitude) × 2° (latitude) grid cells over the world and their mean values are
524   indicated as 'std_mean' on each figure.

5   Regional and global dust DRE based on size-resolved DREE dataset

526   After the validation of *DREE-integration* method in Section 4, we use the *DREE-integration*

527   method to calculate regional and global dust DRE in this section. There are three main objectives

528   in this section: (1) the most important objective throughout this section is to demonstrate the

529   usefulness of the size-resolved DREE dataset for calculating regional and global dust DRE for any

530   given dust PSD; (2) the second objective is to validate the size-resolved DREE dataset by

531   comparing with regional dust DREE reported by field studies based on satellite and ground-based

532   observations (section 5.1); (3) the third objective to assess the sensitivity of dust DRE to DAOD

533   spatial pattern (section 5.2) as well as dust microphysical properties such as dust PSD, RI and

534   shape (section 5.3).

5.1   Comparison with observation-based regional dust DREE

536   Table 3 shows the comparison of our calculations of clear-sky regional mean SW and LW

537   DREE with those reported by field studies based on satellite and ground-based observations. We

538 first calculated regional mean dust DRE using the *DREE-integration* method, then divided by the

539 corresponding regional mean DAOD to get regional mean DREE, and then compared this with

540 observation-based results from previous studies. Comparing DREE allows eliminating differences

541 due to the variation in regional dust loading, optically represented by DAOD.

542   Knowledge of regional dust PSD is necessary for estimating dust DRE regionally. There are

543 several in-situ measurements of dust PSD over Sahara and tropical eastern Atlantic. The state-of-

544 the art airborne observations of Saharan dust from the Fennec field campaign (Fennec-Fresh) and

545 transported Saharan dust over tropical eastern Atlantic within Saharan Air Layer (SAL) from both

546 AER-D and Fennec fieldwork campaigns are adopted (Ryder et al., 2013 a, b, 2018, 2019) (see

547 Figure 7). Both campaigns include giant dust particles, measuring up to $100\mu m$ diameter for AER-

548 D and up to $300\mu m$ for Fennec. The wide coverage of dust diameter in our size-resolved DREE

549 dataset allows for dust DRE calculations for giant dust up to $100\mu m$ over both dust source and

550 transported regions where giant particles are observed in those campaigns. This is an advantage of

551 our size-resolved DREE dataset compared to modeled dust DREE, because climate models

552 generally cut off dust diameter at $20\ \mu m$ and could not sustain coarse dust to remote transport

553 regions due to several missing mechanisms in models (Van Der Does et al., 2018; Drakaki et al.,

554 2022; Meng et al., 2022).

555   The Fennec-Fresh dust PSD includes measurements within 12h of dust uplift in remote

556 Sahara locations. It is used to calculate dust DRE for Saharan dust in this section. In reality, dust

557 over the wide Sahara Desert region (15N~30N, 10W~30E) is not all lifted within 12h, so using

558 Fennec-Fresh to represent dust PSD over the wide Sahara Desert could bias dust size coarse, which

559 could partially explain the warm bias in our DREE[SW] estimation over the Sahara Desert compared

560 to the satellite-based result. Over the tropical Atlantic, both AER-D and Fennec-SAL measured

561 PSD are used to assess the sensitivity of dust DREE to dust PSD. In addition, dust DRE is

562 calculated for three dust RIs to evaluate the sensitivity of dust DREE to dust RI as shown in Table

563 3. Generally, our dust DREE estimations achieve good agreement with observation-based dust

564 DREE. However, there is a significant uncertainty caused by dust RI in DREE, especially for SW.

565 In addition, DRE comparisons between AER-D and Fennec-SAL over the Tropical Atlantic

566 suggests that in-situ measured dust PSD uncertainty leads to a large uncertainty in regional DREE

567 in both SW and LW.

568 Based on the regional DREE study with the state-of-the art RI and PSD, we found $DREE^{SW}$

569 uncertainty could come from both dust RI and dust PSD, while DRE^{LW} uncertainty is mainly from

570 dust PSD.

571 Table 3. Comparison of our DREE estimations for different PSD and RI with Clear-Sky regional SW and LW dust
572 DREE reported by field studies based on satellite and ground-based observations. Specifically, we calculated regional
573 dust DREE for different RI (Min, Mean, Max) and different PSD (AER-D and Fennec-SAL for Tropical Atlantic) and
574 then compare with observation-based results from previous studies. Note, spheroidal dust shape is assumed in our
575 *DREE-integration* DRE calculations.

Shortwave Spectral Range							
Region	Season	Level	Satellite-Based	This study			
			$DREE^{SW}$	$DREE^{SW}$			PSD
				Min RI	Mean RI	Max RI	
Sahara Desert [a] (15N~30N, 10W~30E)	JJA	TOA	0	2.8	16.0	26.6	Fennec-Fresh
Ilorin[f], Nigeria (8.5N, 4.7E)	Annual	TOA	-15 ~ -35	-28.3	-24.1	-19.9	AER-D
				-23.4	-17.7	-12.9	Fennec-SAL
		Surface	-49 ~ -75	-43.1	-51.7	-59.3	AER-D
				-46.0	-57.1	-66.0	Fennec-SAL
Cape Verde[f] (16.7N, 22.9W)	Annual	TOA	-36 ~ -48	-42.3	-38.0	-33.7	AER-D
				-36.6	-30.8	-26.0	Fennec-SAL
		Surface	-68 ~ -90	-59.6	-68.7	-77.7	AER-D
				-61.5	-74.6	-85.3	Fennec-SAL
Tropical Atlantic [b] (10N~30N, 20W-45W)	JJA	TOA	-28	-44.6	-39.9	-35.3	AER-D
				-38.4	-32.1	-27.0	Fennec-SAL
		Surface	-82.1	-61.1	-71.9	-81.7	AER-D
				-64.4	-78.5	-90.0	Fennec-SAL
Tropical Atlantic [c] (15N~25N,15W~45W)	JJA	TOA	-35	-41.2	-36.3	-31.5	AER-D
				-35.1	-28.5	-23.1	Fennec-SAL
		Surface	-65	-57.9	-68.6	-78.1	AER-D
				-61.2	-75.1	-86.3	Fennec-SAL
Longwave Spectral Range							

Region	Season	Level	Satellite-Based DREE^{LW}	This study DREE^{LW}			PSD
				Min RI	Mean RI	Max RI	
Sahara Desert [a] (15N~30N, 10W~30E)	JJA	TOA	11~26	13.4	11.8	11.4	Fennec-Fresh
North Africa [d-e] (15N~35N, 18W~40E)	JJA	TOA	15~22	14.4	12.8	12.4	Fennec-Fresh
Tropical Atlantic [b] (10N~30N, 20W~45W)	JJA	TOA	10.5	8.2	8.1	8.5	AER-D
				13.1	11.8	11.6	Fennec-SAL
Cape Verde [g] (16.7N, 22.9W)	Sept	Surface	16	8.0	11.8	15.1	AER-D
				13.0	17.0	19.8	Fennec-SAL
(a) Patadia et al. (2009). (b) Song et al. (2018). (c) Li et al. (2004). (d) Zhang and Christopher (2003). (e) Brindley and Russell (2009). (f) Zhou et al. (2005). (g) Hansell et al. (2010)							

5.2 Global dust clear-sky DRE based on different DAOD climatology

The DAOD is the most important factor in determining dust DRE. As illustrated in Song et al. (2021), the DAOD retrieved from different satellite sensors have a large difference in terms of magnitude and spatial distribution. To evaluate how the current DAOD uncertainty affects dust DRE estimations, the global dust DRE computed based on monthly mean DAOD climatology retrieved from CALIOP observations and MODIS observations are compared in this section. To separate the effect of DAOD from other factors, we use the same dust PSD, RI and shape in the two sets of dust DRE calculations in this section. Specifically, we use the Fennec-Fresh PSD for three major dust source regions (i.e., Sahara (14-30°N, 15°W-30°E), Middle East (10-35°N, 40-85°E) and eastern Asia (30-50°N, 75-130°E), they are indicated by three black boxes in Figure 10) and use AER-D PSD for other regions (hereafter Campaign-PSD, see Table 5). The MeanSWRI-MeanLWRI-Spheroid dust model described in Table 1 is used to represent dust RI and shape.

The two DAOD climatological datasets result in distinct dust DRE spatial pattern as shown in Figure 10, which is consistent with the DAOD spatial patterns shown in Figure 1 suggesting CALIOP DAOD is more concentrated over 'dust belt' regions than MODIS DAOD. The global mean dust DRE^{SW}, DRE^{LW} and DRE^{NET} based on the two DAOD climatology are significantly

593   different (Table 4), which is mainly caused by two factors. The first is the difference in DAOD

594   magnitude. The CALIOP-based global mean DAOD is 0.032, while MODIS-based is 0.047. The

595   other factor is the difference in DAOD spatial pattern. After we scale dust DRE to the same global

596   mean DAOD ($\overline{DAOD} = 0.03$) to eliminate the effect of DAOD magnitude difference (values in

597   parentheses in Table 4), the DRE^{SW} difference reduced from 0.55 W m^{-2} (-0.69 vs. -1.24 W m^{-2})

598   to 0.15 W m^{-2} (-0.64 vs. -0.79 W m^{-2}). Similarly, differences in DRE^{LW} and DRE^{NET} also reduce

599   significantly. It indicates that the global mean DAOD magnitude difference is more important than

600   the subtle difference in spatial pattern. Nevertheless, after scaling to the same global mean DAOD

601   there is still more than 10% difference between the two dust DRE^{SW}, with CALIOP-based being

602   the more positive one. This is probably because CALIOP-based DAOD is more concentrated over

603   dust sources where dust aerosols induce less negative or even positive DRE^{SW} (For example the

604   positive DRE^{SW} over the Sahara Desert and Arabia shown in Figure 10), which result in a less

605   negative global mean DRE^{SW} than MODIS.

606
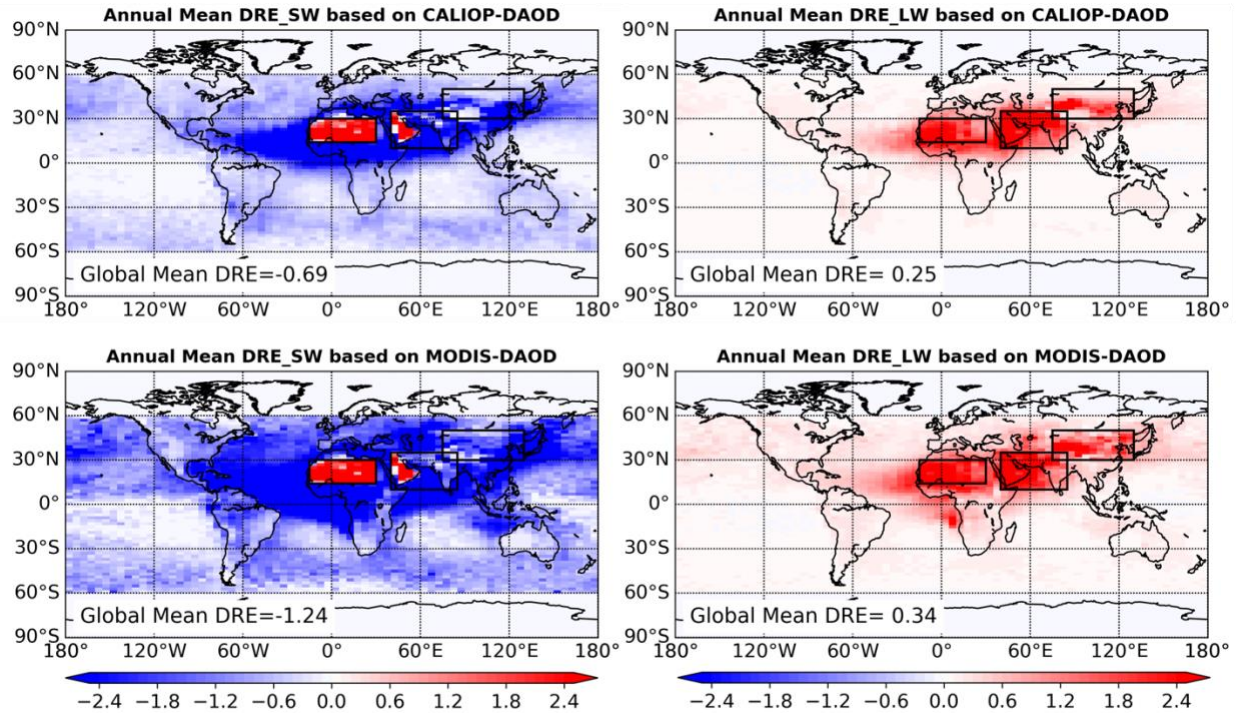
607 Figure 10. Annual mean dust DRE global distribution based on CALIOP-based and MODIS-based DAOD
608 climatology. MeanSWRI-MeanLWRI-Spheroid dust model are used to represent dust RI and shape in the calculation.
609 Campaign-PSD is used to represent dust PSD, specifically, Fennec-Fresh PSD is used to represent dust PSD over the
610 three major dust source regions indicated by three black boxes. AER-D PSD is used to represent dust PSD over other
611 regions.

612 Table 4. Globally annual mean DAOD, DRE^{SW}, DRE^{LW} and DRE^{NET} based on CALIOP DAOD and MODIS DAOD
613 climatology. Note, values in the parentheses are for the two DAOD scaled to the same value of 0.03.

	$\overline{DAOD}$	$\overline{DRE^{SW}}$ [Wm^{-2}]	$\overline{DRE^{LW}}$ [Wm^{-2}]	$\overline{DRE^{NET}}$ [Wm^{-2}]
CALIOP	0.032 (0.03)	−0.69 (−0.64)	0.25 (0.23)	−0.44 (−0.41)
MODIS	0.047 (0.03)	−1.24 (−0.79)	0.34 (0.22)	−0.90 (−0.57)

614

5.3 Global dust clear-sky DRE based on different dust PSD

616   In the section 5.2, we showed the dust DRE based on the Campaign-PSD. As aforementioned,

617 one of the main advantages of our size-resolved DREE is that it can be combined with different

618 dust PSDs to estimate the dust DRE. To demonstrate this, we calculate another set of dust DRE

619 based on the Kok2017-PSD. Table 5 describes the two dust PSDs used for global dust DRE

620 calculations and their references. Kok2017-PSD is a globally averaged dust PSD and used to

621 represent dust PSD for each dusty grid cell. It is constrained with observations and includes coarse

622 dust particles up to $20\mu m$. Although our primary goal here is to demonstrate the capability of our

623 size-resolved DREE, the comparison between the two DRE can also help us understand the

624 impacts of dust PSD uncertainty on the dust DRE estimation. Moreover, we also investigate the

625 sensitivity of DRE to dust RI and dust shape explicitly in this section. The same DAOD

626 climatology (CALIOP-based DAOD climatology) is used for dust DRE calculations to eliminate

627 the impact of dust loading difference.

628   Several recent observation-constrained dust PSDs (e.g., Di Biagio et al., 2020, Adebiyi et

629 al., 2020) suggest that dust size is coarser than Kok2017-PSD. As such, Kok2017-PSD is used to

630 represent the lower limit of the observation-based global dust PSD to investigate the sensitivity of

631 dust DRE to dust PSD. The Campaign-PSD is purely based on aircraft in-situ measurements and

632   the aircraft was extensively equipped to measure giant particles with diameter larger than $20\mu m$.

633   We use the dust PSD measured over Sahara (from the Fennec field campaign) to represent dust

634   PSD over three major dust source regions and use dust PSD measured in the Saharan Air Layer

635   over the tropical eastern Atlantic (from AER-D field campaign) to represent dust PSD over dust

636   transport regions. Of course, representing the spatial and temporal variation of global dust PSD

637   with only two PSDs from the field campaigns is only a crude approximation due to the lack of

638   PSD measurements. Dust aerosol over the three wide dust source regions may not be all uplifted

639   within 12 hours as in the Fennec-Fresh measurements, in addition, dust size after long-range

640   transport could be a bit finer than dust PSD measured over tropical eastern Atlantic (Weinzierl et

641   al., 2017). Thus, Campaign-PSD likely represents the upper limit of the observation-based global

642   dust PSD for the investigation of sensitivity to dust PSD. By contrast, the climate models miss

643   most of coarse dust (D>5 μm) in the atmosphere (Adebiyi and Kok, 2020), as a result, the purely

644   modeled dust PSD without observational constraints will lead to a substantially different dust DRE.

645   Therefore, the sensitivity test to dust PSD conducted in this study can only represent the

646   uncertainty induced by the current understanding of observation-based dust PSD.

647   Table 5. The two observation-based dust PSDs used in DRE calculations (see Figure 7).

PSD	Description	Reference
Kok2017-PSD	A globally averaged atmospheric PSD derived from observation constrained globally averaged emitted PSD and model simulated globally averaged dust lifetime. This globally averaged PSD is used to represent dust PSD for each dusty grid cell. Dust diameter is cutoff at $20\mu m$ (Figure 2a in Kok et al.2017).	Kok et al. (2017)
Campaign-PSD	Fennec-Fresh PSD is used for three major dust source regions (i.e., Sahara (14-30°N, 15°W-30°E), Middle East (10-35°N, 40-85°E) and eastern Asia (30-50°N, 75-130°E)), which are indicated by the three black boxes in Figure 10. AER-D PSD is used for other regions.	Ryder et al. (2013a, b, 2018, 2019)

648

649   We calculated dust DRE of each grid cell ($DRE_{i,j}$) using *DREE-integration* method based

650   on the dust PSD described in Table 5. Global mean dust DRE was then calculated by averaging

651   dust $DRE_{i,j}$ weighted by its surface area. Figure 11 shows the global mean DRE^{SW}, DRE^{LW} and

652   DRE^{NET} at TOA, surface, and in the atmosphere calculated based on the two sets of PSDs.

653   Obviously, Kok2017-PSD leads to stronger cooling effect in SW and weaker warming effect in

654   LW at TOA compared to Campaign-PSD, which is consistent with the fact that Kok2017-PSD is

655   finer than the Campaign-PSD. In addition, we explicitly include the effects of dust RI and dust

656   shape on DRE in Figure 11. Comparison of uncertainty induced by dust PSD, RI and shape

657   suggests that dust RI uncertainty leads to the largest uncertainty in dust DRE, particularly RI

658   uncertainty induces more than 40% uncertainty in DRE^{SW} estimations in the atmosphere (Figure

659   12). Dust PSD is also important for quantifying dust DRE, we found that the observation-based

660   dust PSD uncertainty induces around 15%~20% uncertainty in dust DRE at TOA and in the

661   atmosphere. Dust non-sphericity causes a negligible uncertainty in global mean dust DRE, in line

662   with previous studies e.g., Raisanen et al. (2013) and Colarco et al. (2014).

663

664
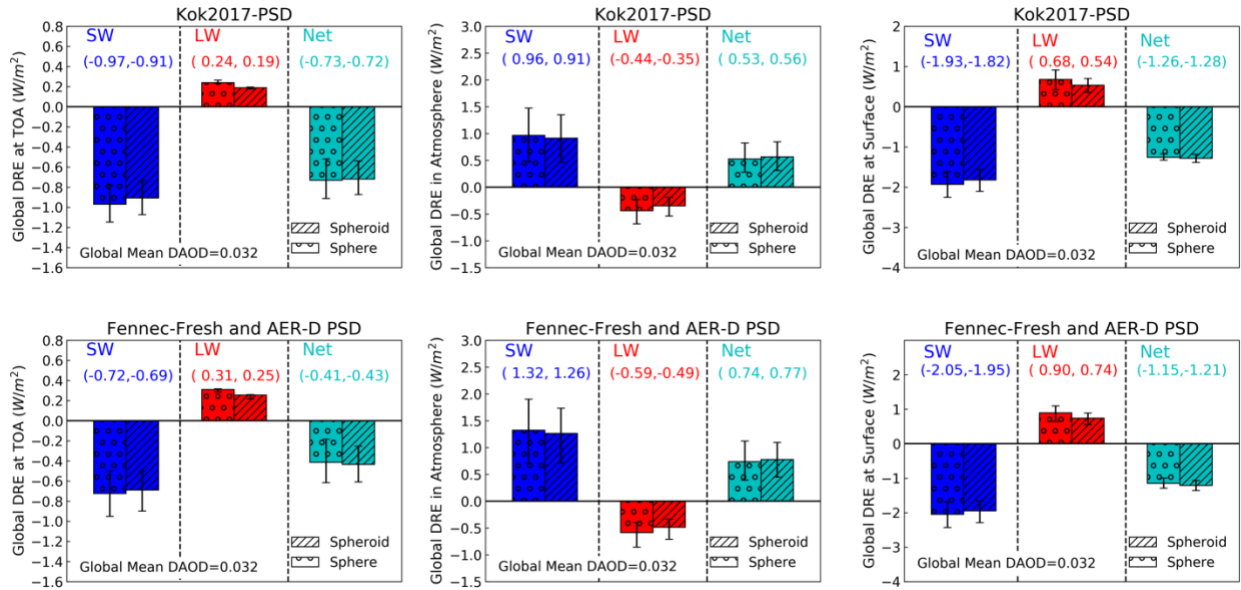
665 Figure 11. Globally annual mean clear-sky DRE^{SW}, DRE^{LW} and DRE^{NET} at TOA, in the atmosphere and surface
666 calculated based on the two PSDs described in Table 5. The two rows represent dust DRE based on two PSDs. Error
667 bars indicate uncertainty induced by dust RI uncertainty. Different types of bars indicate dust DRE based on different
668 dust shapes. This figure explicitly separates the impacts of different dust microphysical properties on dust DRE. Two
669 values in parenthesis on each plot represent spherical (left) and spheroidal (right) dust DRE corresponding to mean
670 RI.
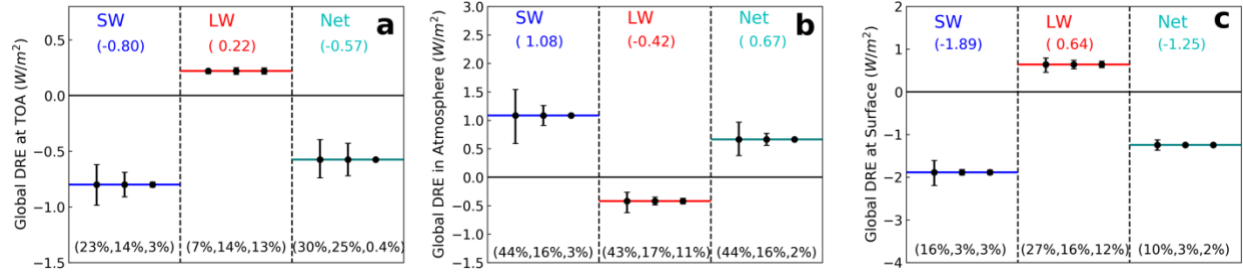
Figure 12. Comparison of uncertainty induced by dust RI, PSD and shape in DRE[SW], DRE[LW] and DRE[NET] at TOA (**a**), in the atmosphere (**b**) and surface (**c**). The horizontal lines in each plot represent global mean DRE[SW] (blue line in the left column), DRE[LW] (red line in the middle column) and DRE[NET] (green line in the right column) averaged over two dust PSDs (i.e., Kok2017-PSD and Campaign-PSD) based on MeanRI-Spheroid dust model. The three error bars in each column represent DRE uncertainty induced by dust RI (left), dust PSD (middle) and dust shape (right). Accordingly, the percentage values on the bottom represent the percentage uncertainty induced by dust RI, PSD and shape, respectively.

It is tempting to compare our global mean dust DRE with results reported in Kok et al. (2017). But it must be noted that the global mean dust DRE shown in Figure 11 is for *clear sky* only, while the global mean dust DRE reported in Kok et al. (2017) is for *all sky*. The all-sky dust DRE can be separated into contributions from clear-sky and cloudy-sky portions (Myhre et al., 2020):

$$DRE_{all-sky} = (1 - CF) \times DRE_{clear-sky} + CF \times DRE_{cloudy-sky}, \qquad (8)$$

where CF is cloud fraction, $DRE_{clear-sky}$ is dust DRE simulated under the case of removing all clouds, $DRE_{cloudy-sky}$ is the dust DRE assuming whole grid is covered by clouds. To compare our global mean dust DRE[SW] based on Kok2017-PSD with the results reported in Kok et al. (2017), we convert our clear-sky $DRE_{clear-sky}^{SW}$ to $DRE_{all-sky}^{SW}$ by using MODIS L3 monthly mean cloud fraction. Specifically, we multiply $DRE_{clear-sky}^{SW}$ by (1-CF) for each grid cell and then calculate global annual mean values. In this process, we neglect the cloudy-sky dust DRE[SW] portion because the annual mean cloudy-sky dust DRE[SW] is estimated to be very small, around −0.04 (Zhang et al., 2016). Finally, our estimated global mean $DRE_{all-sky}^{SW}$ corresponding to DAOD=0.03 is around −0.34 Wm[-2]. Although it is comparable to the −0.48 Wm[-2] from Kok et al. 2017, the following differences between the two studies must be kept in mind when interpreting the results. First, the

693 rough conversion from global mean $DRE^{SW}_{clear-sky}$ to global mean $DRE^{SW}_{all-sky}$ is subject to the

694 approximation of global mean $DRE_{cloudy-sky} \sim 0$ and the MODIS L3 cloud fraction could be

695 different from modeled cloud fraction used in Kok et al. (2017). Second, the two studies use

696 different dust RI. For example, the imaginary part of RI at 550nm in this study ranges from 0.00061

697 to 0.003, while that in Kok et al. (2017) ranges from 0.0014 as used in GEOS-Chem and GISS

698 model based on Sinyuk et al., (2003) to 0.003 as used in WRF-Chem based on Zhao et al., (2010).

699 Third, in this study Kok2017-PSD is used to represent dust PSD in each dusty grid and applied to

700 our size-resolved dust DREE dataset to calculate global dust DRE. In contrast, the model-

701 simulated dust DREE in Kok et al. (2017) has reduced cooling from SW scattering and enhanced

702 warming from SW absorption effects because the short lifetime of coarse dust in models

703 concentrates these particles over bright deserts. Fourth, the two studies use different dust shape

704 models, Kok et al. (2017) accounts for more nonspherical shape model (i.e., tri-axial ellipsoids).

705 Here we do not compare our global mean $DRE^{LW}_{clear-sky}$ with $DRE^{LW}_{all-sky}$ suggested in Kok et al.

706 (2017) because that the lack of knowledge in $DRE^{LW}_{cloudy-sky}$ prevent us to convert $DRE^{LW}_{clear-sky}$

707 to $DRE^{LW}_{all-sky}$. Moreover, the two studies use different dust vertical profile, which is critical for

708 DRE^{LW} estimations. For instance, dust vertical profile in Kok et al. (2017) is purely based on model

709 simulations, while this study constrains dust vertical profile with CALIOP observations.

710 Considering all these factors, it is hard to tell if the comparison is fair.

711 **6 Summary and Conclusion**

712   This study developed a clear-sky size-resolved dust DREE dataset in both SW and LW

713 based on CALIOP-based dust DAOD climatology and dust vertical distributions. The dataset

714 contains global monthly mean dust DREE at TOA and surface with 5° (longitude) × 2° (latitude)

715   spatial resolution for 10 size bins ranging from $0.1\mu m$ to $100\mu m$ diameter, for three state-of-the

716   art dust RI representing more, mean and less absorptive dust, and for two dust shapes representing

717   spherical and spheroidal dust, respectively.

718   The size-resolved DREE dataset allows us to calculate dust DRE of any DAOD

719   climatology and dust PSD efficiently by using the *DREE-integration* method presented in section

720   4.1 without involving radiative transfer simulations. The *DREE-integration* method is proven to

721   be in great agreement with *conventional* DRE calculations. With the *DREE-integration*

722   methodology, we firstly calculated clear-sky regional mean $DREE^{SW}$ and $DREE^{LW}$ over the Sahara

723   Desert and tropical Atlantic. The comparison of our calculations with those reported by field

724   studies based on satellite and ground-based observations shows reasonable agreement. Secondly,

725   we estimated global mean dust DRE with two satellite-based DAOD climatological datasets and

726   two different global dust PSDs. We found that the global mean DAOD magnitude difference

727   between the two DAOD climatological datasets is more important than the subtle difference in

728   spatial pattern. Nevertheless, after scaling to the same global mean DAOD there is still more than

729   10% difference between the two dust DRE^{SW}, with CALIOP-based being the more positive one.

730   Moreover, our results explicitly show the uncertainty induced by each dust microphysical property

731   (i.e., dust PSD, RI and shape) separately. When DAOD is constrained: (a) Dust non-sphericity

732   induces negligible effect on dust DRE estimations; (b) The current understanding of observation-

733   based dust PSD induces relatively large uncertainty (15%~20%) in dust DRE at TOA and in the

734   atmosphere (c) Dust RI turns out to be the most important factor in determining dust DRE,

735   particularly in SW. This implies that better understanding of dust mineral composition and RI will

736   significantly improve our understanding in dust DRE in the future.

737

Data availability. The size-resolved dust DREE dataset and the codes to calculate dust DRE for any given dust PSD and DAOD are available at

'https://drive.google.com/drive/folders/15_e28Y9JiSWiJnIM_2flEmt2u6i9phEY?usp=sharing'

    CALIOP- and MODIS-based DAOD climatological datasets are available at

'https://drive.google.com/drive/folders/1aQVupe7govPwR6qmsqUbR4fJQsp1DBCX?usp=sharing'

Author Contribution. QS and ZZ conceived the scientific ideas. QS did the analysis and completed the initial draft of the manuscript. ZZ, HY, JK, CDB, SA, JZ and JD gave many suggestions for the study and contributed significantly to the revision of the manuscript.

Conflict interests. The authors declare that they have no conflict of interest.

Acknowledgement:

    We would like to thank Dr. Claire L. Ryder for providing the Fennec and AER-D dust PSDs. Qianqian Song and Zhibo Zhang cordially acknowledge the funding support from the Future Investigators in NASA Earth and Space Science and Technology (FINESST). Zhibo Zhang's research is supported by NASA grant (80NSSC20K0130) from the CALIPSO and CloudSat program. S. Albani received funding from MIUR (Progetto Dipartimenti di Eccellenza 2018-2022). The computations in this study were performed at the UMBC High Performance Computing Facility (HPCF). The facility is supported by the US National Science Foundation through the MRI program (grant nos. CNS-0821258 and CNS-1228778) and the SCREMS program (grant no. DMS-0821311), with substantial support from UMBC.

References

Adebiyi, A. A. and Kok, J. F.: Climate models miss most of the coarse dust in the atmosphere, Sci. Adv., 6, eaaz9507, https://doi.org/10.1126/sciadv.aaz9507, 2020.

Adebiyi, A. A., Kok, J. F., Wang, Y., Ito, A., Ridley, D. A., Nabat, P., and Zhao, C.: Dust Constraints from joint Observational-Modelling-experiMental analysis (DustCOMM): Comparison with measurements and model simulations, Atmos. Chem. Phys., 20, 829–863, https://doi.org/10.5194/acp-20-829-2020, 2020.

Albrecht, B. A.: Aerosols, Cloud Microphysics, and Fractional Cloudiness, Science (80-.)., 245, 1227–1230, https://doi.org/DOI 10.1126/science.245.4923.1227, 1989.

Balkanski, Y., Schulz, M., Claquin, T., and Guibert, S.: Reevaluation of Mineral aerosol radiative forcings suggests a better agreement with satellite and AERONET data, Atmos. Chem. Phys., 7, 81–95, https://doi.org/10.5194/acp-7-81-2007, 2007.

Di Biagio, C., Formenti, P., Balkanski, Y., Caponi, L., Cazaunau, M., Pangui, E., Journet, E., Nowak, S., Caquineau, S., Andreae O, M., Kandler, K., Saeed, T., Piketh, S., Seibert, D., Williams, E., and Doussin, J. F. C.: Global scale variability of the mineral dust long-wave refractive index: A new dataset of in situ measurements for climate modeling and remote sensing, Atmos. Chem. Phys., 17, 1901–1929, https://doi.org/10.5194/acp-17-1901-2017, 2017.

Di Biagio, C., Formenti, P., Balkanski, Y., Caponi, L., Cazaunau, M., Pangui, E., Journet, E., Nowak, S., Andreae, M. O., Kandler, K., Saeed, T., Piketh, S., Seibert, D., Williams, E., and Doussin, J. F.: Complex refractive indices and single-scattering albedo of global dust aerosols in the shortwave spectrum and relationship to size and iron content, Atmos. Chem. Phys., 19, 15503–15531, https://doi.org/10.5194/acp-19-15503-2019, 2019.

Di Biagio, C., Balkanski, Y., Albani, S., Boucher, O., and Formenti, P.: Direct Radiative Effect by Mineral Dust Aerosols Constrained by New Microphysical and Spectral Optical Data, Geophys. Res. Lett., 47, e2019GL086186, https://doi.org/doi:10.1029/2019GL086186, 2020.

Brindley, H. E. and Russell, J. E.: An assessment of Saharan dust loading and the corresponding cloud-free longwave direct radiative effect from geostationary satellite observations, J. Geophys. Res. Atmos., 114, https://doi.org/10.1029/2008JD011635, 2009.

Choobari, O. A., P. Zawar-Reza, and Sturman, A.: The global distribution of mineral dust and its impacts on the climate system: A review, Atmos. Res., 138, 152–165, https://doi.org/10.1016/j.atmosres.2013.11.007, 2014.

Colarco, P. R., Nowottnick, E. P., Randles, C. A., Yi, B. Q., Yang, P., Kim, K. M., Smith, J. A., and Bardeen, C. G.: Impact of radiatively interactive dust aerosols in the NASA GEOS-5 climate model: Sensitivity to dust particle shape and refractive index, J. Geophys. Res., 119, 753–786, https://doi.org/10.1002/2013jd020046, 2014.

Van Der Does, M., Knippertz, P., Zschenderlein, P., Harrison, R. G., and Stuut, J.-B. W.: The mysterious long-range transport of giant mineral dust particles, Sci. Adv., 4, 1–9, 2018.

Dubovik, O., Sinyuk, A., Lapyonok, T., Holben, B. N., Mishchenko, M., Yang, P., Eck, T. F., Volten, H., Munoz, O., Veihelmann, B., van der Zande, W. J., Leon, J. F., Sorokin, M., and Slutsker, I.: Application of spheroid models to account for aerosol particle nonsphericity in remote sensing of desert dust, J. Geophys. Res., 111, https://doi.org/Artn D11208 10.1029/2005jd006619, 2006.

Dufresne, J. L., Gautier, C., and Ricchiazzi, P.: Longwave scattering effects of mineral aerosols, J. Atmos. Sci., 59, 1959–1966, https://doi.org/10.1175/1520-0469(2002)059<1959:LSEOMA>2.0.CO;2, 2002.

807   García, O. E., Díez, A. M., Expósito, F. J., Díaz, J. P., Dubovik, O., Dubuisson, P., Roger,
808   J. C., Eck, T. F., Sinyuk, A., Derimian, Y., Dutton, E. G., Schafer, J. S., Holben, B., and García,
809   C. A.: Validation of AERONET estimates of atmospheric solar fluxes and aerosol radiative forcing
810   by ground-based broadband measurements, J. Geophys. Res. Atmos., 113,
811   https://doi.org/10.1029/2008JD010211, 2008.

812   Gelaro, R., McCarty, W., Suárez, M. J., Todling, R., Molod, A., Takacs, L., Randles, C.
813   A., Darmenov, A., Bosilovich, M. G., Reichle, R., Wargan, K., Coy, L., Cullather, R., Draper, C.,
814   Akella, S., Buchard, V., Conaty, A., da Silva, A. M., Gu, W., Kim, G. K., Koster, R., Lucchesi, R.,
815   Merkova, D., Nielsen, J. E., Partyka, G., Pawson, S., Putman, W., Rienecker, M., Schubert, S. D.,
816   Sienkiewicz, M., and Zhao, B.: The modern-era retrospective analysis for research and
817   applications, version 2 (MERRA-2), J. Clim., 30, 5419–5454, https://doi.org/10.1175/JCLI-D-16-
818   0758.1, 2017.

819   Ginoux, P., Prospero, J. M., Gill, T. E., Hsu, N. C., and Zhao, M.: Global-scale attribution
820   of anthropogenic and natural dust sources and their emission rates based on MODIS Deep Blue
821   aerosol products, https://doi.org/10.1029/2012RG000388, 1 September 2012.

822   Gkikas, A., Proestakis, E., Amiridis, V., Kazadzis, S., Di Tomaso, E., Tsekeri, A., Marinou,
823   E., Hatzianastassiou, N., and Pérez Garciá-Pando, C.: ModIs Dust AeroSol (MIDAS): A global
824   fine-resolution dust optical depth data set, Atmos. Meas. Tech., 14, 309–334,
825   https://doi.org/10.5194/amt-14-309-2021, 2021.

826   Hansell, R. A., Tsay, S. C., Ji, Q., Hsu, N. C., Jeong, M. J., Wang, S. H., Reid, J. S., Liou,
827   K. N., and Ou, S. C.: An assessment of the surface longwave direct radiative effect of airborne
828   Saharan dust during the NAMMA field campaign, J. Atmos. Sci., 67, 1048–1065,
829   https://doi.org/10.1175/2009JAS3257.1, 2010.

830   Hsu, N. C., Jeong, M.-J., Bettenhausen, C., Sayer, A. M., Hansell, R., Seftor, C. S., Huang,
831   J., and Tsay, S.-C.: Enhanced Deep Blue aerosol retrieval algorithm: The second generation, J.
832   Geophys. Res. Atmos., 118, 9296–9315, https://doi.org/https://doi.org/10.1002/jgrd.50712, 2013.

833   Huang, Y., Kok, J. F., Kandler, K., Lindqvist, H., Nousiainen, T., Sakai, T., Adebiyi, A.,
834   and Jokinen, O.: Climate Models and Remote Sensing Retrievals Neglect Substantial Desert Dust
835   Asphericity, Geophys. Res. Lett., 47, https://doi.org/10.1029/2019GL086592, 2020.

836   van de Hulst, H. C.: Light scattering by small particles, Wiley, Hoboken,NJ, 1957.

837   Huneeus, N., Schulz, M., Balkanski, Y., Griesfeller, J., Prospero, J., Kinne, S., Bauer, S.,
838   Boucher, O., Chin, M., Dentener, F., Diehl, T., Easter, R., Fillmore, D., Ghan, S., Ginoux, P., Grini,
839   A., Horowitz, L., Koch, D., Krol, M. C., Landing, W., Liu, X., Mahowald, N., Miller, R., Morcrette,
840   J. J., Myhre, G., Penner, J., Perlwitz, J., Stier, P., Takemura, T., and Zender, C. S.: Global dust
841   model intercomparison in AeroCom phase i, Atmos. Chem. Phys., 11, 7781–7816,
842   https://doi.org/10.5194/acp-11-7781-2011, 2011.

843   Kato, S., Rose, F. G., Sun-Mack, S., Miller, W. F., Chen, Y., Rutan, D. A., Stephens, G.
844   L., Loeb, N. G., Minnis, P., Wielicki, B. A., Winker, D. M., Charlock, T. P., Stackhouse, P. W.,
845   Xu, K. M., and Collins, W. D.: Improvements of top-of-atmosphere and surface irradiance
846   computations with CALIPSO-, CloudSat-, and MODIS-derived cloud and aerosol properties, J.
847   Geophys. Res., 116, https://doi.org/Artn D19209 10.1029/2011jd016050, 2011.

848   Kaufman, Y. J., Koren, I., Remer, L. A., Tanré, D., Ginoux, P., and Fan, S.: Dust transport
849   and deposition observed from the Terra-Moderate Resolution Imaging Spectroradiometer
850   (MODIS) spacecraft over the Atlantic Ocean, J. Geophys. Res. D Atmos., 110, 1–16,
851   https://doi.org/10.1029/2003JD004436, 2005.

852   Koffi, B., Schulz, M., Bréon, F. M., Griesfeller, J., Winker, D., Balkanski, Y., Bauer, S.,

Berntsen, T., Chin, M., Collins, W. D., Dentener, F., Diehl, T., Easter, R., Ghan, S., Ginoux, P., Gong, S., Horowitz, L. W., Iversen, T., Kirkevg, A., Koch, D., Krol, M., Myhre, G., Stier, P., and Takemura, T.: Application of the CALIOP layer product to evaluate the vertical distribution of aerosols estimated by global models: AeroCom phase i results, https://doi.org/10.1029/2011JD016858, 2012.

Kok, J. F., Ridley, D. A., Zhou, Q., Miller, R. L., Zhao, C., Heald, C. L., Ward, D. S., Albani, S., and Haustein, K.: Smaller desert dust cooling effect estimated from analysis of dust size and abundance, Nat. Geosci., 10, 274–278, https://doi.org/10.1038/Ngeo2912, 2017.

Li, F., Vogelmann, A. M., and Ramanathan, V.: Saharan dust aerosol radiative forcing measured from space, J. Clim., 17, 2558–2571, https://doi.org/Doi 10.1175/1520-0442(2004)017<2558:Sdarfm>2.0.Co;2, 2004.

Mahowald, N., Albani, S., Kok, J. F., Engelstaeder, S., Scanza, R., Ward, D. S., and Flanner, M. G.: The size distribution of desert dust aerosols and its impact on the Earth system, https://doi.org/10.1016/j.aeolia.2013.09.002, 1 December 2014.

Meloni, D., di Sarra, A., Di Iorio, T., and Fiocco, G.: Influence of the vertical profile of Saharan dust on the visible direct radiative forcing, J. Quant. Spectrosc. Radiat. Transf., 93, 397–413, https://doi.org/10.1016/j.jqsrt.2004.08.035, 2005.

Meloni, D., Junkermann, W., di Sarra, A., Cacciani, M., De Silvestri, L., Di Iorio, T., Estellés, V., Gómez-Amo, J. L., Pace, G., and Sferlazzo, D. M.: Altitude-resolved shortwave and longwave radiative effects of desert dust in the Mediterranean during the GAMARF campaign: Indications of a net daily cooling in the dust layer, J. Geophys. Res., 120, 3386–3407, https://doi.org/10.1002/2014JD022312, 2015.

Meng, Z. K., Yang, P., Kattawar, G. W., Bi, L., Liou, K. N., and Laszlo, I.: Single-scattering properties of tri-axial ellipsoidal mineral dust aerosols: A database for application to radiative transfer calculations, J. Aerosol Sci., 41, 501–512, https://doi.org/10.1016/j.jaerosci.2010.02.008, 2010.

Mlawer, E. J. and Clough, S. A.: Shortwave and longwave enhancements in the rapid radiative transfer model, Proc. Seventh Atmos. Radiat. Meas. Sci. Team Meet., 409–413, 1998.

Mlawer, E. J., Taubman, S. J., Brown, P. D., Iacono, M. J., and Clough, S. A.: Radiative transfer for inhomogeneous atmospheres: RRTM, a validated correlated-k model for the longwave, J. Geophys. Res. Atmos., 102, 16663–16682, https://doi.org/10.1029/97jd00237, 1997.

Myhre, G., Grini, A., Haywood, J. M., Stordal, F., Chatenet, B., Tanre, D., Sundet, J. K., and Isaksen, I. S. A.: Modeling the radiative impact of mineral dust during the Saharan Dust Experiment (SHADE) campaign, J. Geophys. Res., 108, https://doi.org/Artn 8579 10.1029/2002jd002566, 2003.

Myhre, G., Samset, B. H., Mohr, C. W., Alterskjær, K., Balkanski, Y., Bellouin, N., Chin, M., Haywood, J., Hodnebrog, O., Kinne, S., Lin, G., Lund, M. T., Penner, J. E., Schulz, M., Schutgens, N., Skeie, R. B., Stier, P., Takemura, T., and Zhang, K.: Cloudy-sky contributions to the direct aerosol effect, Atmos. Chem. Phys., 20, 8855–8865, https://doi.org/10.5194/acp-20-8855-2020, 2020.

Patadia, F., Yang, E. S., and Christopher, S. A.: Does dust change the clear sky top of atmosphere shortwave flux over high surface reflectance regions?, Geophys. Res. Lett., 36, https://doi.org/10.1029/2009GL039092, 2009.

Pu, B. and Ginoux, P.: How reliable are CMIP5 models in simulating dust optical depth?, Atmos. Chem. Phys., 18, 12491–12510, https://doi.org/10.5194/acp-18-12491-2018, 2018.

Raisanen, P., Haapanala, P., Chung, C. E., Kahnert, M., Makkonen, R., Tonttila, J., and

899 Nousiainen, T.: Impact of dust particle non-sphericity on climate simulations, Q. J. R. Meteorol.
900 Soc., 139, 2222–2232, https://doi.org/10.1002/qj.2084, 2013.

901 Remer, L. A., Kaufman, Y. J., Tanré, D., Mattoo, S., Chu, D. A., Martins, J. V, Li, R. R.,
902 Ichoku, C., Levy, R. C., Kleidman, R. G., Eck, T. F., Vermote, E., and Holben, B. N.: The MODIS
903 aerosol algorithm, products, and validation, J. Atmos. Sci., 62, 947–973,
904 https://doi.org/10.1175/JAS3385.1, 2005.

905 Ryder, C. L., Highwood, E. J., Lai, T. M., Sodemann, H., and Marsham, J. H.: Impact of
906 atmospheric transport on the evolution of microphysical and optical properties of Saharan dust,
907 Geophys. Res. Lett., 40, 2433–2438, https://doi.org/10.1002/grl.50482, 2013a.

908 Ryder, C. L., Highwood, E. J., Rosenberg, P. D., Trembath, J., Brooke, J. K., Bart, M.,
909 Dean, A., Crosier, J., Dorsey, J., Brindley, H., Banks, J., Marsham, J. H., McQuaid, J. B.,
910 Sodemann, H., and Washington, R.: Optical properties of Saharan dust aerosol and contribution
911 from the coarse mode as measured during the Fennec 2011 aircraft campaign, Atmos. Chem. Phys.,
912 13, 303–325, https://doi.org/10.5194/acp-13-303-2013, 2013b.

913 Ryder, C. L., Marenco, F., Brooke, J. K., Estelles, V., Cotton, R., Formenti, P., McQuaid,
914 J. B., Price, H. C., Liu, D., Ausset, P., Rosenberg, P. D., Taylor, J. W., Choularton, T., Bower, K.,
915 Coe, H., Gallagher, M., Crosier, J., Lloyd, G., Highwood, E. J., and Murray, B. J.: Coarse-mode
916 mineral dust size distributions, composition and optical properties from AER-D aircraft
917 measurements over the tropical eastern Atlantic, Atmos. Chem. Phys., 18, 17225–17257,
918 https://doi.org/10.5194/acp-18-17225-2018, 2018.

919 Ryder, C. L., Highwood, E. J., Walser, A., Seibert, P., Philipp, A., and Weinzierl, B.:
920 Coarse and Giant Particles are Ubiquitous in Saharan Dust Export Regions and are Radiatively
921 Significant over the Sahara, Atmos. Chem. Phys. Discuss., https://doi.org/10.5194/acp-2019-421,
922 2019.

923 Sakai, T., Nagai, T., Zaizen, Y., and Mano, Y.: Backscattering linear depolarization ratio
924 measurements of mineral, sea-salt, and ammonium sulfate particles simulated in a laboratory
925 chamber, Appl. Opt., 49, 4441–4449, 2010.

926 Satheesh, S. K. and Ramanathan, V.: Large differences in tropical aerosol forcing at the
927 top of the atmosphere and Earth's surface, Nature, 405, 60–63, https://doi.org/10.1038/35011039,
928 2000.

929 Sinyuk, A., Torres, O., and Dubovik, O.: Combined use of satellite and surface
930 observations to infer the imaginary part of refractive index of Saharan dust, Geophys. Res. Lett.,
931 30, https://doi.org/10.1029/2002GL016189, 2003.

932 Sokolik, I. N., Toon, O. B., and Bergstrom, R. W.: Modeling the radiative characteristics
933 of airborne mineral aerosols at infrared wavelengths, J. Geophys. Res., 103, 8813–8826,
934 https://doi.org/Doi 10.1029/98jd00049, 1998.

935 Song, Q., Zhang, Z., Yu, H., Kato, S., Yang, P., Colarco, P., Remer, L. A., and Ryder, C.
936 L.: Net radiative effects of dust in the tropical North Atlantic based on integrated satellite
937 observations and in situ measurements, Atmos. Chem. Phys., 18, https://doi.org/10.5194/acp-18-
938 11303-2018, 2018.

939 Song, Q., Zhang, Z., Yu, H., Ginoux, P., and Shen, J.: Global dust optical depth climatology
940 derived from CALIOP and MODIS aerosol retrievals on decadal timescales: regional and
941 interannual variability, Atmos. Chem. Phys., 21, 13369–13395, https://doi.org/10.5194/acp-21-
942 13369-2021, 2021.

943 Stamnes, K., Tsay, S.-C., Wiscombe, W., and Jayaweera, K.: Numerically stable algorithm
944 for discrete-ordinate-method radiative transfer in multiple scattering and emitting layered media,

Appl. Opt., 27, 2502, https://doi.org/10.1364/ao.27.002502, 1988.

Tegen, I. and Lacis, A. A.: Modeling of particle size distribution and its influence on the radiative properties of mineral dust aerosol, J. Geophys. Res. Atmos., 101, 19237–19244, https://doi.org/10.1029/95jd03610, 1996.

Tegen, I., Lacis, A. A., and Fung, I.: The influence on climate forcing of mineral aerosols from disturbed soils, Nature, 380, 419–422, https://doi.org/10.1038/380419a0, 1996.

Textor, C., Schulz, M., Guibert, S., Kinne, S., Balkanski, Y., Bauer, S., Berntsen, T., Berglen, T., Boucher, O., Chin, M., Dentener, F., Diehl, T., Easter, R., Feichter, H., Fillmore, D., Ghan, S., Ginoux, P., Gong, S., Kristjansson, J. E., Krol, M., Lauer, A., Lamarque, J. F., Liu, X., Montanaro, V., Myhre, G., Penner, J., Pitari, G., Reddy, S., Seland, O., Stier, P., Takemura, T., and Tie, X.: Analysis and quantification of the diversities of aerosol life cycles within AeroCom, Atmos. Chem. Phys., 6, 1777–1813, 2006.

Twomey, S.: The influence of pollution on the shortwave albedo of clouds, J. Atmos. Sci., 34, 1149–1152, 1977.

Voss, K. K. and Evan, A. T.: A New Satellite-Based Global Climatology of Dust Aerosol Optical Depth, J. Appl. Meteorol. Climatol., 59, 83–102, https://doi.org/10.1175/JAMC-D-19, 2020.

Vouk, V.: Projected area of convex bodies [3], https://doi.org/10.1038/162330a0, 1948.

Weinzierl, B., Ansmann, A., Prospero, J. M., Althausen, D., Benker, N., Chouza, F., Dollner, M., Farrell, D., Fomba, W. K., Freudenthaler, V., Gasteiger, J., Gross, S., Haarig, M., Heinold, B., Kandler, K., Kristensen, T. B., Mayol-Bracero, O. L., Muller, T., Reitebuch, O., Sauer, D., Schafler, A., Schepanski, K., Spanu, A., Tegen, I., Toledano, C., and Walser, A.: THE SAHARAN AEROSOL LONG-RANGE TRANSPORT AND AEROSOL-CLOUD-INTERACTION EXPERIMENT Overview and Selected Highlights, Bull. Am. Meteorol. Soc., 98, 1427–1451, https://doi.org/10.1175/Bams-D-15-00142.1, 2017.

Winker, D. M., Vaughan, M. A., Omar, A., Hu, Y., Powell, K. A., Liu, Z., Hunt, W. H., and Young, S. A.: Overview of the CALIPSO mission and CALIOP data processing algorithms, J. Atmos. Ocean. Technol., 26, 2310–2323, https://doi.org/10.1175/2009JTECHA1281.1, 2009.

Wiscombe, W. J.: Improved Mie Scattering Algorithms, Appl. Opt., 19, 1505–1509, https://doi.org/Doi 10.1364/Ao.19.001505, 1980.

Wu, M., Liu, X., Yu, H., Wang, H., Shi, Y., Yang, K., Darmenov, A., Wu, C., Wang, Z., Luo, T., Feng, Y., and Ke, Z.: Understanding processes that control dust spatial distributions with global climate models and satellite observations, Atmos. Chem. Phys., 20, 13835–13855, https://doi.org/10.5194/acp-20-13835-2020, 2020.

Yu, H., Kaufman, Y. J., Chin, M., Feingold, G., Remer, L. A., Anderson, T. L., Balkanski, Y., Bellouin, N., Boucher, O., Christopher, S., DeCola, P., Kahn, R., Koch, D., Loeb, N., Reddy, M. S., Schulz, M., Takemura, T., and Zhou, M.: A review of measurement-based assessments of the aerosol direct radiative effect and forcing, Atmos. Chem. Phys., 6, 613–666, 2006.

Yu, H., Chin, M., Remer, L. A., Kleidman, R. G., Bellouin, N., Bian, H., and Diehl, T.: Variability of marine aerosol fine-mode fraction and estimates of anthropogenic aerosol component over cloud-free oceans from the Moderate Resolution Imaging Spectroradiometer (MODIS), J. Geophys. Res. Atmos., 114, https://doi.org/10.1029/2008JD010648, 2009.

Yu, H., Chin, M., Winker, D. M., Omar, A. H., Liu, Z., Kittaka, C., and Diehl, T.: Global view of aerosol vertical distributions from CALIPSO lidar measurements and GOCART simulations: Regional and seasonal variations, J. Geophys. Res. Atmos., 115, 1–19, https://doi.org/10.1029/2009JD013364, 2010.

991   Yu, H., Tan, Q., Chin, M., Remer, L. A., Kahn, R. A., Bian, H., Kim, D., Zhang, Z., Yuan,
992 T., Omar, A. H., Winker, D. M., Levy, R. C., Kalashnikova, O., Crepeau, L., Capelle, V., and
993 Chédin, A.: Estimates of African Dust Deposition Along the Trans-Atlantic Transit Using the
994 Decadelong Record of Aerosol Measurements from CALIOP, MODIS, MISR, and IASI, J.
995 Geophys. Res. Atmos., 124, 7975–7996, https://doi.org/10.1029/2019JD030574, 2019.

996   Yu, H., Yang, Y., Wang, H., Tan, Q., Chin, M., Levy, R., Remer, L., Smith, S., Yuan, T.,
997 and Shi, Y.: Interannual Variability and Trends of Combustion Aerosol and Dust in Major
998 Continental Outflows Revealed by MODIS Retrievals and CAM5 Simulations During 2003–2017,
999 Atmos. Chem. Phys. Discuss., 1–38, https://doi.org/10.5194/acp-2019-621, 2020.

1000   Zhang, J. L. and Christopher, S. A.: Longwave radiative forcing of Saharan dust aerosols
1001 estimated from MODIS, MISR, and CERES observations on Terra, Geophys. Res. Lett., 30,
1002 https://doi.org/Artn 2188 10.1029/2003gl018479, 2003.

1003   Zhang, Z. B., Meyer, K., Yu, H. B., Platnick, S., Colarco, P., Liu, Z. Y., and Oreopoulos,
1004 L.: Shortwave direct radiative effects of above-cloud aerosols over global oceans derived from 8
1005 years of CALIOP and MODIS observations, Atmos. Chem. Phys., 16, 2877–2900,
1006 https://doi.org/10.5194/acp-16-2877-2016, 2016.

1007   Zhao, C., Liu, X., Leung, L. R., Johnson, B., McFarlane, S. A., Gustafson, W. I., Fast, J.
1008 D., and Easter, R.: The spatial distribution of mineral dust and its shortwave radiative forcing over
1009 North Africa: Modeling sensitivities to dust emissions and aerosol size treatments, Atmos. Chem.
1010 Phys., 10, 8821–8838, https://doi.org/10.5194/acp-10-8821-2010, 2010.

1011   Zheng, J., Zhang, Z., Garnier, A., Yu, H., Song, Q., Wang, C., Dubuisson, P., and Di Biagio,
1012 C.: The thermal infrared optical depth of mineral dust retrieved from integrated CALIOP and IIR
1013 observations, Remote Sens. Environ., 270, https://doi.org/10.1016/j.rse.2021.112841, 2022.

1014   Zhou, M., Yu, H., Dickinson, R. E., Dubovik, O., and Holben, B. N.: A normalized
1015 description of the direct effect of key aerosol types on solar radiation as estimated from Aerosol
1016 Robotic Network aerosols and Moderate Resolution Imaging Spectroradiometer albedos, J.
1017 Geophys. Res. D Atmos., 110, 1–10, https://doi.org/10.1029/2005JD005909, 2005.
1018